

# Electrospun Polymer Nanofibers: Mechanical and Thermodynamic Perspectives

Arkadii Arinstein, Eyal Zussman

Department of Mechanical Engineering, Technion–Israel Institute of Technology, Haifa 32000, Israel

Correspondence to: E. Zussman (E-mail: meeyal@tx.technion.ac.il)

Received 24 December 2010; revised 8 March 2011; accepted 9 March 2011; published online 2011

DOI: 10.1002/polb.22247

**ABSTRACT:** This article reviews and discusses some open problems concerning polymer materials of reduced sizes and dimensions. Such objects exhibit exceptional physical properties when compared with their macroscopic counterparts. More specifically, abrupt increases in polymer nanofiber elastic modulus have been observed when diameters drop below a certain value. In addition, temperature dependence of elastic modulus is highly influenced by fiber diameter. Mechanical (macroscopic) analyses have failed to provide satisfactory explanations for the mechanisms ruling such features, calling for detailed microscopic examination of the systems in question. A hypothesis bridging the current knowledge gaps is presented. The key element of this hypothesis is based on

confinement of the supermolecular microstructure of polymer nanofibers and its dominant role in the deformation process. This suggestion challenges the commonly held view suggesting that surface effects are the most significant parameters impacting mechanical and thermodynamic nanofiber behaviors. The review will focus on the mechanical and thermodynamic properties of electrospun polymer nanofibers, selected as representatives of nanoscale polymer objects. © 2011 Wiley Periodicals, Inc. *J Polym Sci Part B: Polym Phys* 49: 691–707, 2011

**KEYWORDS:** electrospinning; fibers; mechanical properties; nanotechnology; thermal properties

**INTRODUCTION** Polymer nanofibers attract much attention due to their fundamental importance in a broad range of applications. Reduction of polymer fiber diameter into the nanometer range gives rise to a set of favorable properties including an increase in surface-to-volume ratio,<sup>1,2</sup> variations in wetting behavior,<sup>3,4</sup> controlled release of drugs,<sup>5</sup> high anisotropic electrical conductivity,<sup>6,7</sup> and enhanced light scattering and photoluminescence.<sup>8</sup>

Polymer nanofibers are intrinsically different from common bulk in that they demonstrate size-dependent behavior, a well-known phenomenon frequently observed in nano-objects. Experimental studies have demonstrated the effect of size on the mechanical and thermodynamic properties of nano-objects, as seen with the elastic moduli of hollow fibers<sup>9</sup> and electrospun nanofibers,<sup>10–14</sup> which sharply increase below a certain fiber diameter, as well as shifts in object melting temperatures.<sup>15,16</sup> Similarly, thickness and surface interactions of ultrathin polymer films (the film thickness is in the order of  $2R_g$  of a polymer chain, or less) highly influence their glass transition and melting temperatures,<sup>17–19</sup> polymer dynamics in the glassy state,<sup>20</sup> crystallization kinetics and degree of crystallinity,<sup>21–23</sup> phase behavior,<sup>24</sup> and morphology.<sup>25,26</sup>

For all the above examples, the portion of “surface material” is comparable with the bulk, due to extremely small object size, therefore, the ansatz claiming “nano-object = bulk +

surface” seems relevant for such systems from a physical point of view. However, in certain experimental systems,<sup>27,28</sup> the size-dependent behavior of nanofibers bearing considerably higher transversal size ( $\sim 500$  nm) refute the size-dependence ansatz and require additional expressions to explain their behavior.

The present review will focus on the mechanical and thermodynamic properties of electrospun polymer nanofibers, selected as representatives of nanoscale polymer objects. The parameters of the electrospinning process critical in influencing fiber structures will be described, followed by the exploration of a number of atypical mechanical and thermodynamic properties of polymer nanofibers. This review will also concentrate on elastic modulus enhancement, as well as on melting temperature shifts among semicrystalline polymer nanofibers. Finally, a review of the current physical models attempting to clarify nanofiber size-dependent behavior will be presented.

## ELECTROSPINNING OF POLYMER NANOFIBERS

Polymer-based nanofibers are fabricated by means of electrospinning, during which a polymer solution, typically semidilute in nature,<sup>29</sup> is extruded from a spinneret, and by a strong electric field a jet is formed at the tip (see Fig. 1). The resulting jet then undergoes extreme elongation and thinning, in the order

**Arkadii Arinstein** received his MSc degree in Theoretical Physics from Tomsk State University in 1977 and Ph.D. degree in Theoretical and Mathematical Physics from the Landau Institute for Theoretical Physics of the USSR Academy of Sciences in Moscow in 1982. For many years he worked in the Semenov Institute for Chemical Physics of the Russian Academy of Sciences in Moscow, where received DSc (habilitation) degree in Chemical Physics in 1995. Now he is the Research-Professor Associate at the Technion-Israel Institute of Technology. Arinstein's research interests include statistical physics of polymers, non-linear phenomena in disordered systems. Last 5 years his research is related with nanotechnology and are devoted to polymer nanofibers.



**Eyal Zussman** has been at the Department of Mechanical Engineering, Technion—Israel Institute of Technology since 1994. He received his doctoral degree in mechanical engineering from the Technion in 1992. From 1992 to 1994, he was a postdoctoral fellow at the Technical University in Berlin, Germany. Zussman's research interests are in the nanoscale polymer fabrication and mechanics.



of  $10^5$ , accompanied by a strain rate of the order  $10^3 \text{ s}^{-1}$ , leading to stretching and orientation of the polymer chains. Stretching along the jet can be monitored by in-process measurements such as birefringence<sup>30</sup> and Raman techniques.<sup>31</sup> Extremely rapid solvent evaporation occurs with continued jet flow, resulting in the formation of a skin within a few milliseconds, and quenching of the polymer matrix macrostructure, resulting in a nonequilibrium state.<sup>32–34</sup>

Once a firm, solid skin is created, it resists further solvent evaporation, allowing for a considerable amount of solvent to remain trapped within the nanofibers, resulting in relaxation of the nonequilibrium state of the stretched macromolecules. Thus, it is not the fabrication conditions that impact the final state of the polymer matrix of as-spun nanofibers, but rather, solvent evaporation occurring after skin formation. While the transversal scale of spinning fibers is not considerably decreased, the volume freed by solvent evaporation leaves a heterogeneous and porous nanofiber structure [see Figs. 2 and 3(a)].

Theoretical analyses<sup>36,37</sup> confirmed by experimental observations<sup>38–40</sup> have demonstrated that rapid evaporation yields sharp increases in polymer density at the fiber/vapor interface, consequently increasing fiber heterogeneity and porosity (Fig. 2). In this manner, nanofiber skin layers can thicken to a substantial fraction of the fiber's diameter, ensuring its integrity. Continued, slow evaporation of the solvent from the nanofiber core can proceed for several seconds or even minutes, accompanied by further evolution of the nanofibers in both their microstate and macrostate. Thus, by proper selection of the spinning conditions, homogeneously structured electrospun fibers can be generated [see Fig. 3(b)]. In these cases, the relaxation of stretched polymer chains is suppressed, and the effect of fabrication conditions on the final state of polymer matrix of nanofibers is noticeable. In the following sections, the spinnability of various polymer solutions will be considered, the unique flow developed in the jet during electrospinning

will be described, and finally, the stress relaxation process in the as-spun fibers will be discussed.

### Spinnable Polymer Solutions

The dependence of polymer solution viscosity,  $\eta$ , on the solution's relative concentration,  $c/c^*$ , can be categorized along three distinct concentration ranges identified as dilute ( $c/c^* < 1$ ), semidilute unentangled ( $1 < c/c^* < 3$ ), and semidilute entangled ( $c/c^* > 3$ ) [see Fig. 4(a)]. In a semidilute unentangled solution, droplets (aerosol) rather than continuous nanofibers are formed, due to insufficient chain entanglement. Conversely, a semidilute entangled solution ensures elastic jet behavior and formation of continuous nanofibers.

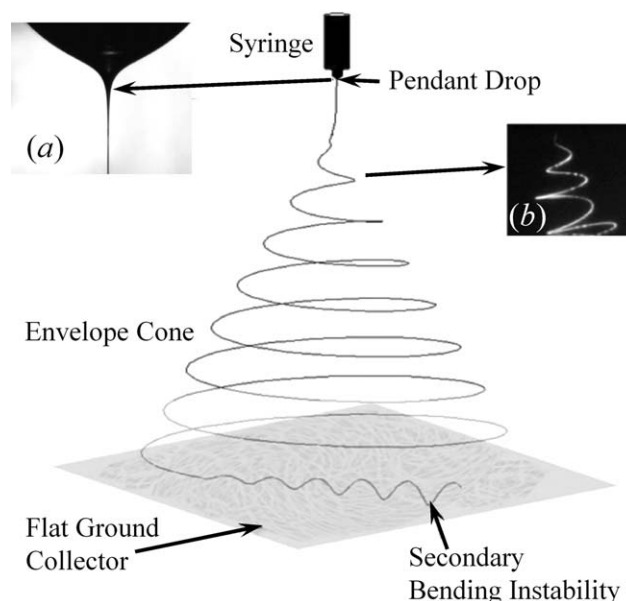


**FIGURE 1** Sketch of the electrospinning process (a) image of the Taylor cone and (b) image of the bending instabilities.

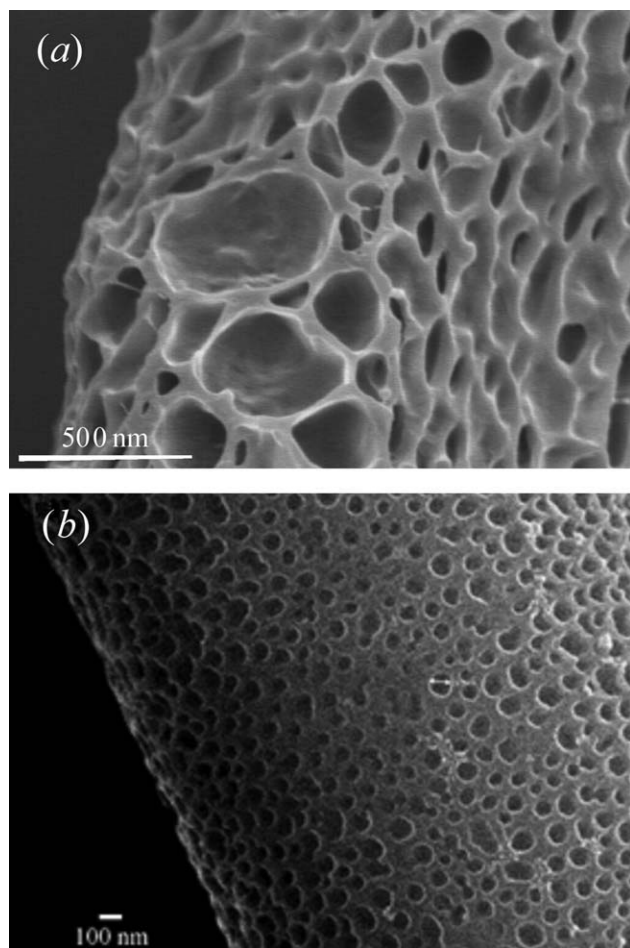


**FIGURE 2** SEM images of electrospun nanofibers made with (a) 6% polycaprolactone (PCL) in dichloromethane/*N,N*-dimethylformamide (85/15). (b) 28 wt % polystyrene (PS) in tetrahydrofuran. From Megelski et al., *Macromolecules*, 2002, 35, 3456–3466, © American Chemical Society, reproduced by permission.<sup>35</sup>

Variations in solution concentrations impact the diameter of the as-spun fiber, despite identical electrospinning processing parameters. The experimental dependence of fiber diameter on polymer concentration for semidilute entangled polymer solutions is presented in Figure 4(b). Based on these experiments, the following scaling relationships for the dependencies of fiber diameter,  $d$ , on the relative concentration  $c/c^*$  and on the zero shear rate viscosity  $\eta_0$  can be derived:

$$d \propto (c/c^*)^{3.1}, \quad \text{and} \quad d \propto \eta_0^{0.72}, \quad (1)$$

which agrees with measurements reported for different types of polymer, resulting in  $d \propto c^{3.41}$  or  $d \propto c^{2.99}$ .<sup>42</sup>

### The Jet Flow

Under the electric field, the solution jet with density,  $\rho$ , viscosity,  $\eta$ , and conductivity and permeability,  $K$  and  $\varepsilon$ , respectively, ejected at a constant flow rate,  $Q$ , is accelerated toward the lower potential electrode (see Fig. 5). The jet's local velocity contains both longitudinal and radial components<sup>43–45</sup>

$$v_z \approx v_0(1 + z/z_0)^2, \quad v_r \approx -v_0(1 + z/z_0) \frac{r}{z_0}, \quad (2)$$

where  $v_0$  is the jet initial velocity, and the characteristic length,  $z_0$ , determines the scale of velocity increase and depends on  $Q$ ,  $\eta$ ,  $K$ , the surface tension,  $\gamma$ , and the electric field.

In a capillary dominated regime, where the capillary number,  $C_a \sim (\eta Q/r_0^2 \gamma)$ , is sufficiently small (typically in the electrospinning  $C_a \sim 10^{-2}$ ),<sup>44</sup> surface tension plays a significant role in shaping the surface of the jet. For example, electrified jets generated in a capillary-dominated regime with  $0.0063 < C_a \leq 0.018$  and large  $\varepsilon$  are hyperbolic-shaped with radius  $r_j(z) \approx r_0/(1 + z/z_0)$  (see Fig. 6). The jet shape in the region near the orifice is elongated and slightly dependent on  $C_a$ , whereas the straight section of the jet demonstrates tighter dependence, where thickness increases with  $C_a$  for a fixed  $z$ .

Although the shape of the inertia-less jets distant from the orifice is hyperbolic for both capillary- ( $C_a \ll 1$ ) and viscosity-dominated ( $C_a \gg 1$ ) regimes, the respective profiles of their axial velocities at the jet cross-section differ. While the cross-section profile of the axial velocity is approximately parabolic, the

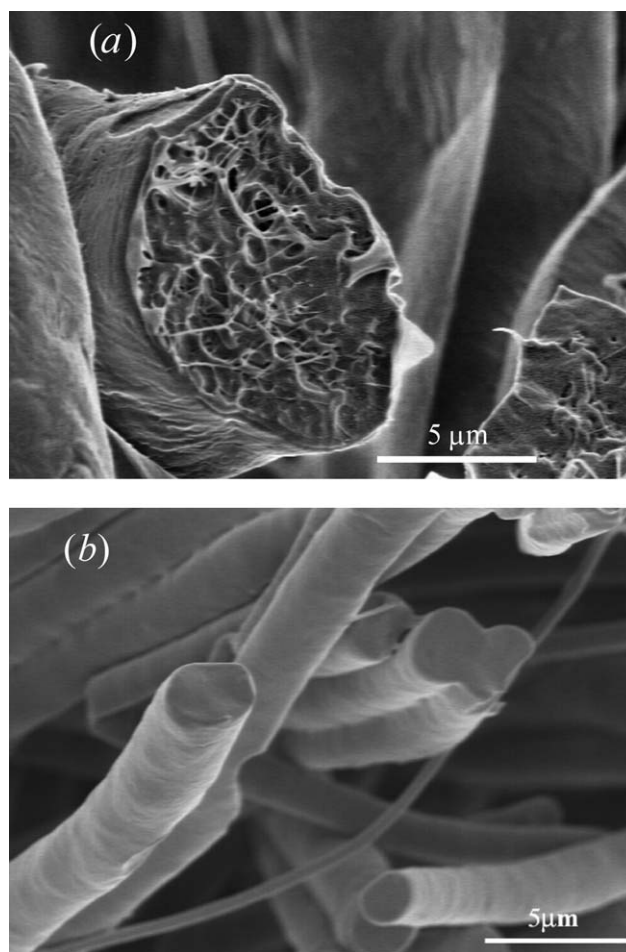


**FIGURE 3** Images of electrospun nanofibers made with 10% PCL ( $M_w = 80,000$ ) in dichloromethane/*N,N*-dimethylformamide (75/25). (a) Heterogeneous fibers fabricated at 20 mL/h, with electric field 0.6 kV/cm. (b) Homogeneous fibers fabricated at 3 mL/h, with electric field 0.63 kV/cm.

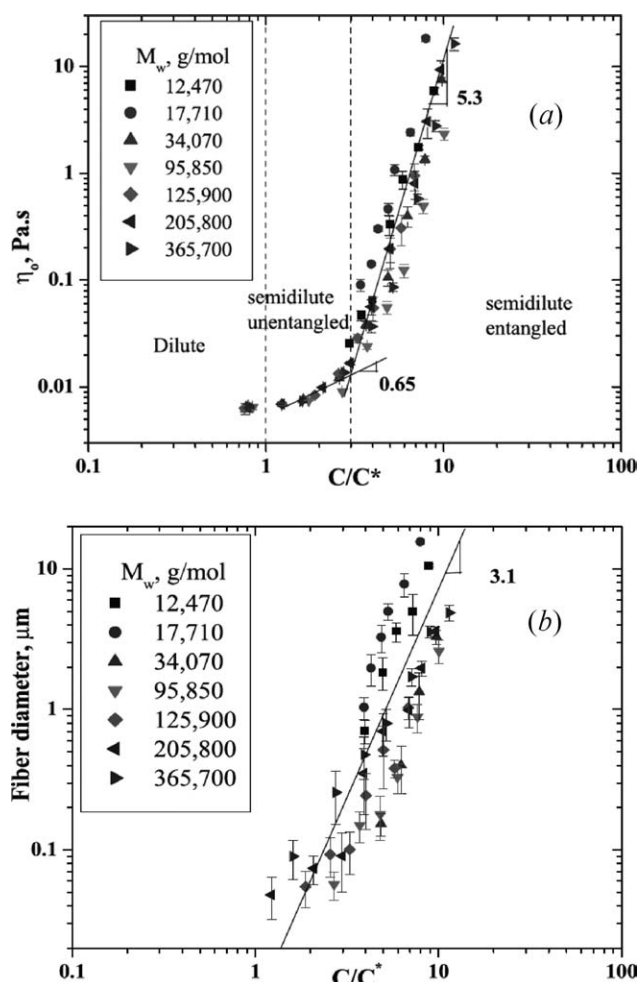


**FIGURE 4** (a) Zero shear rate viscosity  $\eta_0$  versus relative concentration,  $C/C^*$ , for polymethyl methacrylate (PMMA) of different molecular weights ( $M_w$ ) and (b) variation of fiber diameter versus relative concentration,  $C/C^*$ , PMMA of different  $M_w$ . From Gupta et al., *Polymer*, 2005, 46, 4799–4810, © Elsevier, reproduced by permission.<sup>29</sup>

capillary-dominated regime takes on a concave and the viscosity-dominated regime a convex (i.e., Poiseuille-like flow) curvature.

Velocity distributions along the jet have been verified by experimental observations collected by means of optical methods ranging from simple low-speed or static white light imaging of the jet profile near the tip or via more complex techniques such as high-speed bright-field imaging of unique formations in the jet, laser Doppler velocimetry, or fluorescence microscopy. For example, in the velocity measurement presented by Han et al.<sup>46</sup> [see Fig. 7(a)], the jet rapidly accelerates, reaching a velocity of  $\sim 1$  m/s at a distance of 5 mm from the starting point. In doing so, the stretching rate in the transition zone,  $dV/dx$ , lies within  $100$ – $1000$   $\text{s}^{-1}$ . In parallel, the jet diameter decreases very sharply, and is already too small to measure at distances beyond 3 mm of the starting point [see Fig. 7(a)]. Analogous results were obtained by

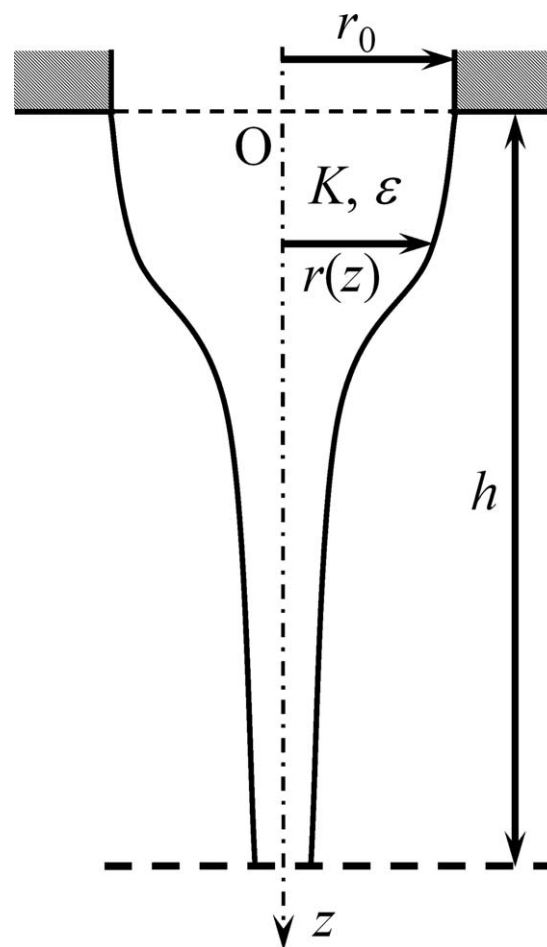


**FIGURE 5** Sketch of a stationary jet of a leaky dielectric issuing from the orifice in a plane electrode, toward a counter electrode, located at distance,  $h$ .  $K$  represents liquid conductivity and  $\epsilon$  denotes permeability.

Bellan et al.<sup>47</sup> [see Fig. 7(b)] who demonstrated a jet velocity of 0.25 m/s at a distance 1 mm from the starting point, corresponding to a stretching rate of  $\sim 300$   $\text{s}^{-1}$ .

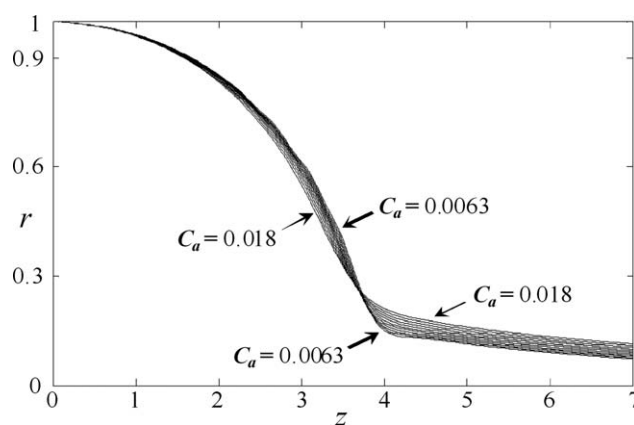


**FIGURE 6** Jet shapes for various capillary numbers,  $Ca$ . From Reznik and Zussman, *Phys. Rev. E*, 2009, 81, 026313, © American Physical Society, reproduced by permission.<sup>44</sup>



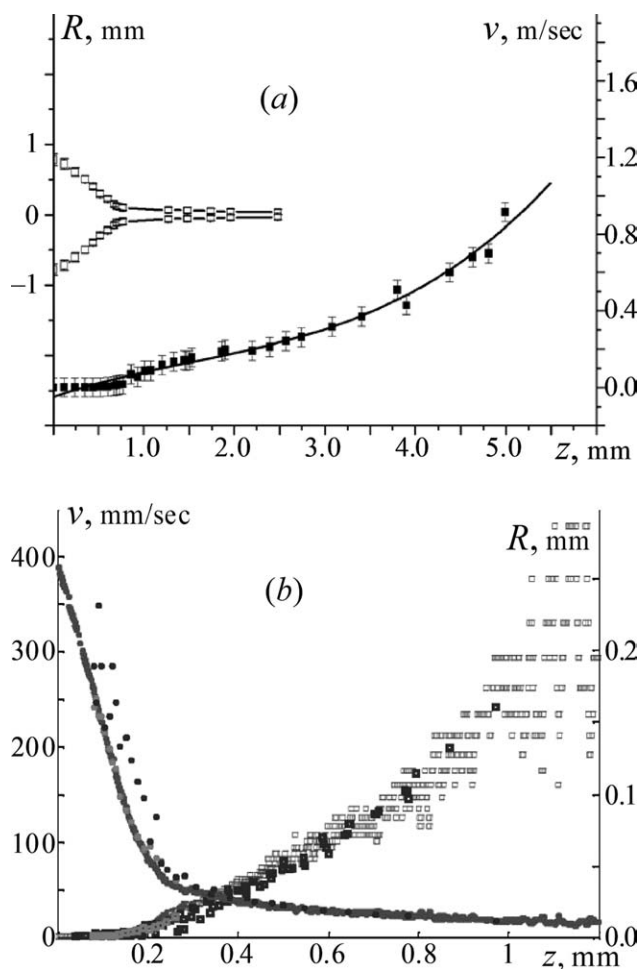


**FIGURE 7** Jet velocity versus distance from starting point (a) Profile of the transition zone following the modified Taylor cone and the beginning of the jet. The cross-sectional radius is shown as  $R = R(z)$ . From Han et al., *Polymer*, 2008, 49, 1651–1658, © Elsevier, reproduced by permission.<sup>46</sup> (b) Velocity and jet radius plotted as a function of the  $z$  position, length along the jet. From Bellan et al., *J. Appl. Phys.*, 2007, 102, © American Institute of Physics, reproduced by permission.<sup>47</sup>

Such extreme polymer solution stretching rates result in a nonequilibrium stretched state of polymer macromolecules. An analogy to the phenomenon of coil-stretch transition of dilute flexible polymers under ultrahigh velocity gradients was drawn by de Gennes<sup>48</sup> and seems suitable for the estimation of the degree of polymer macromolecules stretching. However, the present situation is more complex, as electrospinnability requires semidilute solutions. In such cases, a nonuniform tensile flow acts on the polymeric physical network, where topological links are formed as a result of chain entanglement (a polymeric physical network under very rapid deformation can be regarded as polymer gel). Although the behavior of polymer gels under rapid deformation has been discussed by many authors,<sup>49–53</sup> we are not aware of a solution for the specific problem occurring in the electro-

spinning process, namely local deformation of an elongated network of semidilute polymer solution.

#### Postprocesses Relaxation in Electrospun Nanofibers

As mentioned above, rapid solvent evaporation during electrospinning results in accelerated nanofiber solidification, leading to a nonequilibrium state of the polymer macromolecules. This stretched state is assumed to be stabilized in the solid matrix and can account for the anomalous properties of the nanofibers. The theoretical analysis and simulation performed by Guenther et al.<sup>36</sup> have shown that polymer macromolecules in electrospun fibers are inhomogeneously distributed in the nanofiber cross-section.

Early solvent evaporation, resulting in the formation of a skin, is dictated by the competition between diffusion of solvent into the skin and evaporation of solvent to the surrounding. To estimate the actual evaporation time, a tubular nanofiber,<sup>54–56</sup> filled with solvent, is examined. This system can be considered as an extreme case of the model discussed

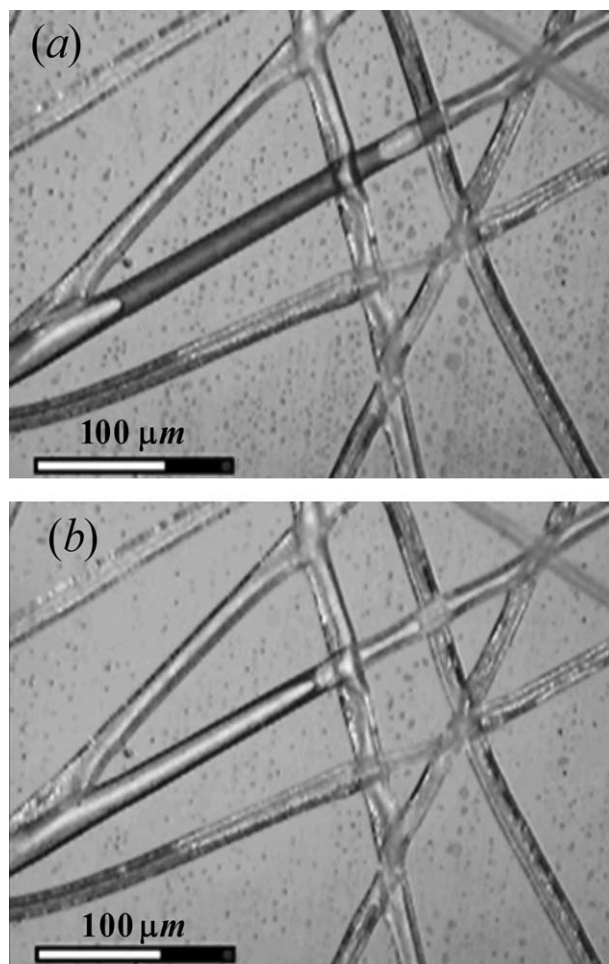


**FIGURE 8** As-spun fiber with a slug of entrapped core solvent (a) A typical image of an as-spun fiber with an entrapped slug bounded by two menisci; and (b) disappearance of this slug as a result of solvent evaporation. From Arinstein and Zussman, *Phys. Rev. E*, 2007, 76, 056303 1–7, © American Physical Society, reproduced by permission.<sup>57</sup>

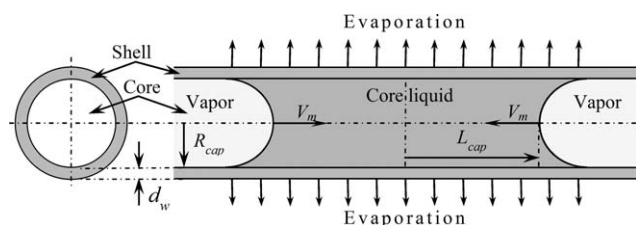


**FIGURE 9** A scheme of the dominant processes determining the evaporation kinetic. From Arinstein and Zussman, Phys. Rev. E, 2007, 76, 056303 1–7, © American Physical Society, reproduced by permission.<sup>57</sup>

by Guenther et al.<sup>36</sup> Use of such tubular nanofibers enables *in situ* tracking of the kinetics of solvent evaporation through the nanofiber shell.

Experimental studies<sup>57,58</sup> describe collection of tubular nanofibers containing entrapped core solvent for observation under an optical microscope, within 10 s of fabrication. Observations of the as-spun nanofibers uncovered capillaries containing many slugs of entrapped core solvent, bound in a vapor phase [see Fig. 8(a)]. The observed slug shortens as evidenced by the menisci approaching each other at a velocity,  $V_m$ , and finally disappears as a result of solvent evaporation [see Fig. 8(b)]. This setup enabled experimental analysis of further evaporation of solvent, encapsulated within the nanofibers, and demonstrated a typical evaporation duration of tens of seconds.

Consideration of the dominant processes affecting solvent evaporation provides a reasonable starting point for determining its kinetics (see Fig. 9).

Core solvent evaporation can occur at both the shell and the menisci. At first glance, it would appear that the latter channel would be dominant, as solvent filtration through the capillary wall is limited by a very low diffusion coefficient ( $D_s \sim 10^{-13} \div 10^{-12} \text{ m}^2/\text{s}$ ).<sup>59</sup> However, when accounting for the ratio of meniscus to capillary wall surface areas, it can be concluded that solvent evaporation at the meniscus surfaces bears limited influence on evaporation kinetics, while solvent filtration through the capillary wall controls the process in question. The process can be described by the following set of equations and boundary conditions. As the fluid motion is inertialess (Reynolds number,  $Re \approx 10^{-6}$ ), and governed by the Stokes equation, and the length of the slug is much larger than its radius,  $L_{\text{cap}} \gg R_{\text{cap}}$ , we can assume a local Poiseuille's flow with pressure gradient  $\partial P/\partial x$ :

$$V(x, t) = -\frac{R_{\text{cap}}^2}{8\eta} \frac{\partial P(x, t)}{\partial x}, \quad (3)$$

where  $V(x, t)$  is the mean velocity of the solvent in the cross-section of a capillary.

The second equation describing the process incorporates the mass conservation law, which accounts for solvent evaporation:

$$\frac{\partial V(x, t)}{\partial x} = -\frac{2D_s}{R_{\text{cap}}d_w} \cdot \frac{1 + \kappa P(x, t)/P(L_{\text{cap}}(t), t)}{1 + \kappa}, \quad (4)$$

where  $R_{\text{cap}}$  and  $d_w$  are the radius of a capillary and thickness of its wall, respectively.

The key element of this equation lies in the varied liquid flux through the capillary wall, stemming from hampered infiltration with decreasing pressure along the capillary. This phenomenon was taken into account in the simplest manner, by representing the pressure drop through a linear function, which equals 1 when  $x = L_{\text{cap}}(t)$ , with a single free dimensionless parameter,  $\kappa$ .

The boundary conditions for eqs 3 and 4 are:

$$\begin{aligned} P(x, t)|_{x=\pm L_{\text{cap}}(t)} &= P_{\text{at}} - 2\gamma/R_{\text{cap}} = P_b, \\ V_m(t) &= V(x, t)|_{x=\pm L_{\text{cap}}(t)} = \pm \partial L_{\text{cap}}(t)/\partial L_{\text{cap}}(t)/\partial t, \\ L_{\text{cap}}(t=0) &= L_0, \end{aligned} \quad (5)$$

where  $P_{\text{at}} = 10^5 \text{ N/m}^2$  is the atmospheric pressure, and  $\gamma$  is the surface tension.

Assuming  $\gamma \propto 50 \times 10^{-3} \text{ N/m}$ ,  $R_{\text{cap}} \propto 10^{-5} \text{ m}$ , and  $2\gamma/R_{\text{cap}} \propto 10^4 \text{ N/m}^2$  ( $\sim 0.1 P_{\text{at}}$ ), we can conclude that the influence of the surface tension on evaporation kinetics is negligible. However, in the case of radial capillary deformation (e.g., due to bending), the influence of surface tension can become significant and result in decreased meniscus displacement rates.

The solution of eqs 3–5 is:

$$\sinh(L_{\text{cap}}(t)/\xi) = \sinh(L_0/\xi) \cdot \exp(-t/\tau) \quad (6)$$

$$V(x, t) = -\frac{\xi \sinh(x/\xi)}{\tau \cosh(L_{\text{cap}}(t)/\xi)} \quad (7)$$

where  $\xi = \frac{1}{4} \sqrt{(1+a)R_{\text{cap}}^3 d_w P_b / a D_s \eta}$  and  $\tau = R_{\text{cap}} d_w / 2D_s$ .

At the initial stage, when  $L_{\text{cap}}(t)/\xi \gg 1$ , eq 6 can be transformed into

$$\exp(L_{\text{cap}}(t)/\xi) = \exp(L_0/\xi) \cdot \exp(-t/\tau) \quad (8)$$

Hence, the meniscus moves at a constant rate,  $-\xi/\tau$ ,

$$\Delta L = L_0 - L_{\text{cap}}(t) \approx \xi t/\tau \quad (9)$$

For the opposite case, when  $t/\tau \gg 1$ , that is,  $L_{\text{cap}}(t)/\xi \ll 1$ , eq 6 is

$$L_{\text{cap}}(t) = \xi \sinh(L_0/\xi) \cdot \exp(-t/\tau) \quad (10)$$

Hence, the meniscus displacement rate decreases exponentially,

$$V_m(t) = \frac{\partial L_{\text{cap}}(t)}{\partial t} \approx -\frac{\xi}{\tau} \sinh(L_0/\xi) \cdot \exp(-t/\tau) \quad (11)$$

This solution reflects the asymptotic behavior at the final evaporation stage. Fitting the experimental data with the aid of eq 6 allows one to estimate the value of characteristic evaporation time,  $\tau$ , which proves to be in the order of  $10\text{--}10^2 \text{ s}$ , during which polymer matrix relaxation is possible. A typical pattern of meniscus displacement and its velocity,  $V_m$ ,

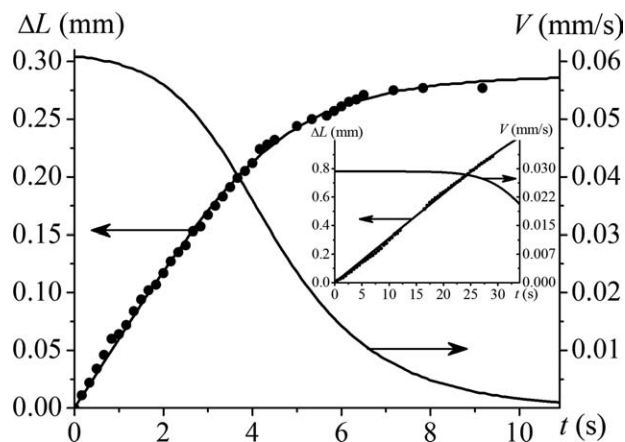


**FIGURE 10** Meniscus displacement and its velocity versus time. The dots display the experimental data and the lines display the theoretical model. The inset displays a set of experimental data for a long slug, where evaporation through the capillary wall is dominant. From Arinstein and Zussman, *Phys. Rev. E*, 2007, 76, 056303 1–7, © American Physical Society, reproduced by permission.<sup>57</sup>

is displayed in Figure 10. Initially, the meniscus moves at a constant rate (eq 9; see Fig. 10 inset for the pattern of a long slug). The velocity then decelerates, and finally, when the distance between the left and right menisci is small, meniscus displacement slowly tapers off. This final evaporation stage is described by eq 10.

In cases of capillary deformation, the influence of solvent surface tension increases, leading to decreased meniscus displacement velocity. This effect has been experimentally observed in cases of deformed fibers (for example, by bending; see Fig. 11).

While the initial evaporation stage could not be observed in the above experiments, extrapolations from subsequent developments and analysis of the entire evaporation process provide information regarding this stage. Tubular fibers are fully

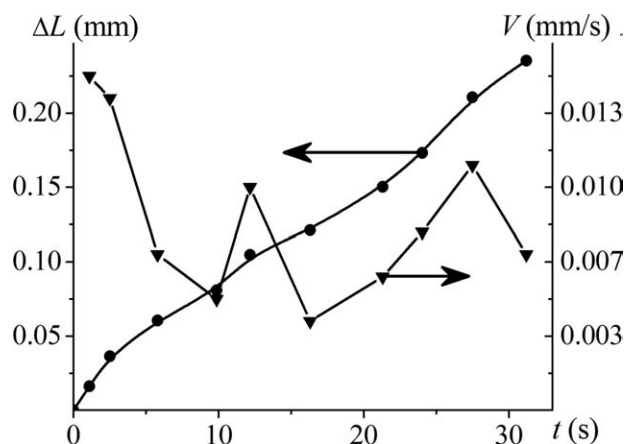


**FIGURE 11** Meniscus displacement (left axis) and its velocity (right axis) vs. time for deformed capillaries. From Arinstein and Zussman, *Phys. Rev. E*, 2007, 76, 056303 1–7, © American Physical Society, reproduced by permission.<sup>57</sup>

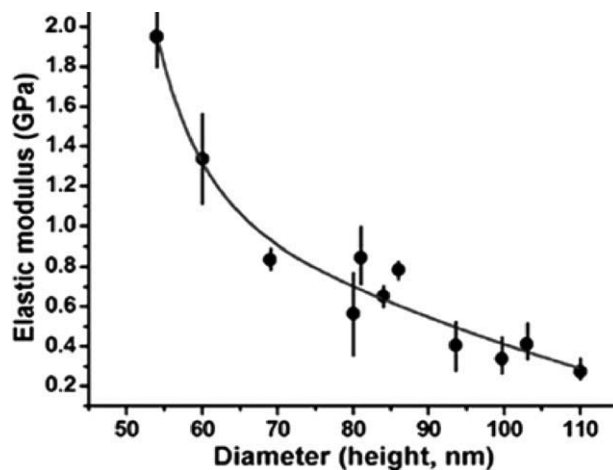


**FIGURE 12** Variation of the measured elastic modulus,  $E$ , for PAMPS (poly-2-acrylamido-2-methyl-1-propanesulfonic acid) electrospun nanofibers as a function of the diameter,  $d$ . From Shin et al., *Appl. Phys. Lett.*, 2006, 89, © American Institute of Physics reproduced by permission.<sup>14</sup>

filled with solvent immediately postfabrication. During the initial stage of evaporation, gas bubbles rise within the tube, breaking the continuous liquid into several slugs. Thereafter, when slugs are relatively long, they can break into many smaller slugs, the starting point for the experimental observations described above. Slug segmentation, accompanied by creation of two new menisci, requires energy, which can be obtained at the expense of the elastic energy accumulated in the fiber shell as a result of solvent evaporation.

Despite the variant evaporation kinetics in tubular and solid-core fibers, the same mechanism can be applied to explain and predict the structure evolution of the tubular nanofibers. The system described above can be considered an extreme solid-core case, that is, one with a sharp polymer density gradient, as the polymer density near the fiber surface is high but significantly lower at the core.<sup>36</sup> Therefore, the kinetics of solvent evaporation in solid-core nanofibers can be considered similar to that of tubular fibers. As expected, evaporation rates in solid-core nanofibers is slower than in tubular ones, due to notable increases in the effective inner fiber solvent viscosity. This evaporation rate can be approximated at the early evaporation stages, using a porous medium model. Nevertheless, the qualitative features of solvent evaporation in solid-core nanofibers remain inherently equivalent to those of tubular nanofibers, implying that the postprocesses in fabricated nanofibers (in particular, the polymer matrix relaxation) determine the final state of polymer macromolecules, thereby significantly affecting the mechanical and thermodynamic properties of polymeric nanofibers.

#### MECHANICAL AND THERMODYNAMIC PROPERTIES OF POLYMER NANOFIBERS

The mechanical and thermodynamic properties of polymer nano-objects show a remarkably regular pattern in comparison with their bulk-related properties. However, these properties sharply vary when object scale drops below a critical threshold (e.g., thickness for films and diameters for fibers). The reason



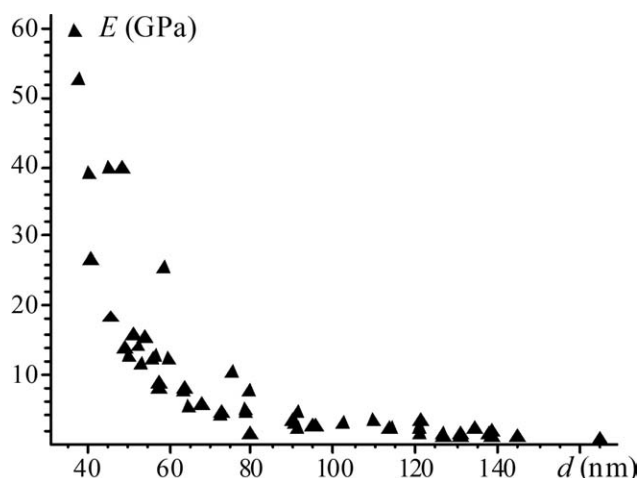


**FIGURE 13** Variation of the measured reduced elastic modulus,  $E$ , of polypyrrole nanotubes, as a function of their outer diameter,  $d$ . From Cuenot et al., Phys. Rev. Lett., 2000, 85, 1690–1693, © the American Physical Society, reproduced by permission.<sup>9</sup>

for the observed size-dependent changes in these properties is poorly understood. Mechanistic models have attributed such behavior, for both two-dimensional and one-dimensional nano-systems, to surface effects.<sup>19,60–63</sup> Although surface phenomena clearly play a role in the final properties of materials of reduced sizes, detailed analyses shows that surface effect alone cannot adequately explain the experimental observations. In the following sections, we first review the mechanical properties of several electrospun fibers and describe the related testing methods. Next, we present experimental results showing the dependence of thermodynamical properties of the fibers, such as glass and melting temperature, on the fiber diameter.

### Mechanical Properties of Polymer Nanofibers

An abrupt increase in the elastic modulus of PAMPS (poly-2-acrylamido-2-methyl-1-propanesulfonic acid) nanofibers<sup>14</sup>

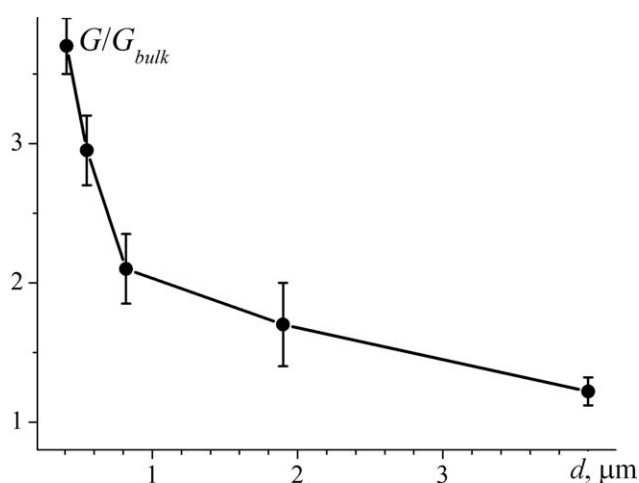


**FIGURE 14** Relative shear modulus  $G/G_{\text{bulk}}$  of electrospun polystyrene nanofibers as a function of fiber diameter,  $d$ , where  $G \propto E$ . From Ji et al., Langmuir, 2006, 22, 1321–1328, © the American Chemical Society, reproduced by permission.<sup>27</sup>

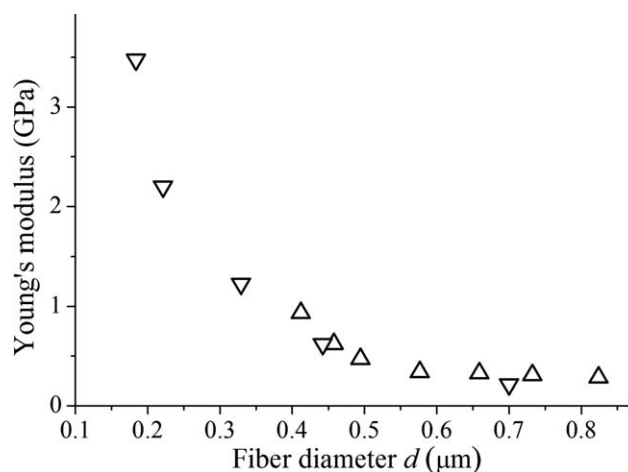


**FIGURE 15** Elastic modulus,  $E$ , of electrospun nylon 6,6 nanofibers vs. fiber diameter,  $d$ , measured using tensile ( $\triangle$ ) and resonant vibration ( $\nabla$ ) tests which utilize uniaxial stretching. From Burman et al., Appl. Phys. Lett., 2008, 93193118, 1–3, © the American Institute of Physics, reproduced by permission.<sup>12</sup>

(see Fig. 12) and polypyrrole nanotubes (see Fig. 13) has been observed when their diameters dropped below 80–100 nm. A similar dependence was observed for electrospun polystyrene<sup>27</sup> and nylon 6,6<sup>11,12</sup> nanofibers (see Figs. 14 and 15), while in the latter case, the crossover to size-dependent behavior was already seen at 500–800 nm.

Measurements of PAMPS nanofibers and polypyrrole nanotubes moduli were performed using the three-point bending technique.<sup>64</sup> The atomic force microscopy (AFM) tip was positioned at the midpoint of the suspended nano-object, for measurement of object deflection (see Fig. 16).

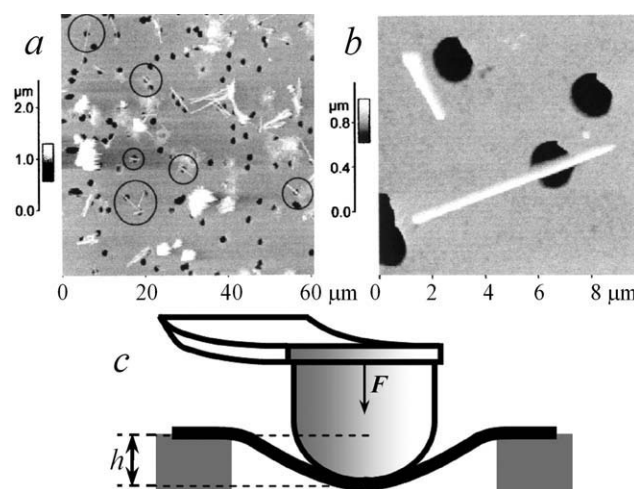


**FIGURE 16** (a) High resolution image of polypyrrole nanotubes dispersed on a PET membrane reveals several tubes crossing pores (encircled). (b) Close-up view of a polypyrrole nanotube suspended over a pore. From Cuenot et al., Phys. Rev. Lett., 2000, 85, 1690–1693, © the American Physical Society, reproduced by permission.<sup>9</sup> (c) A scheme of the Three-Point Bending AFM test, where  $F$  is the applied force and  $h$  is the nanotubes deflection.



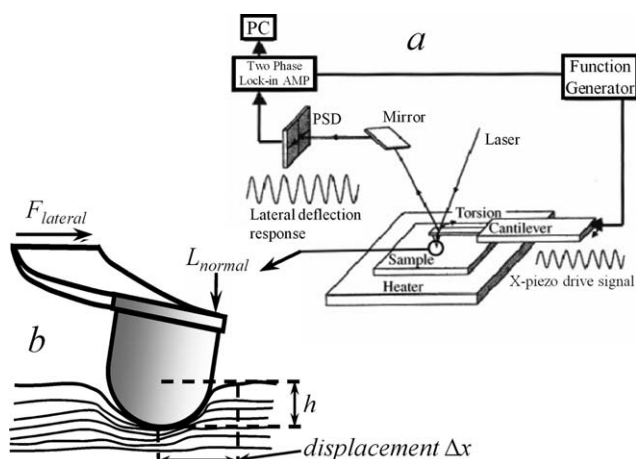


**FIGURE 17** (a) Scheme of Shear modulation force microscopy (SMFM) setup. (b) Detailed view of a cantilever acting on a polymer nanofiber film (indicated by a circle in a). From Ji et al., *Langmuir*, 2006, 22, 1321–1328, © the American Chemical Society, reproduced by permission.<sup>27</sup>

The modulus measurements demonstrated in Figure 14 are based on Shear Modulation Force Microscopy (SMFM). In this technique, a fiber bundle is suspended across the gap of a grating, where the AFM tip is allowed to impinge on the fiber, causing the deformation (see Fig. 17). The modulus measured in this manner is a collective property of a bundle of fibers and can be obtained from the force-distance curve of the AFM probe. Although the resultant recorded shear modulus,  $G$ , relates to the entire fiber bundle, fiber elastic modulus,  $E$ , can be estimated,

$$E = 2(1 + \nu)G, \quad (12)$$

where  $\nu$  is the Poisson's ratio.

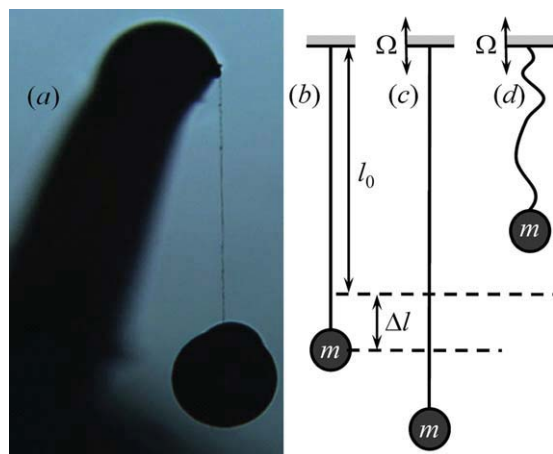


**FIGURE 18** The string pendulum. (a) View of a ball glued to a nanofiber and suspended from a cantilever beam, which is attached to the actuated base ( $\times 100$ ). (b) The equilibrium state, (c) the downward displacement, and (d) the upper displacement of the bob's flight. From Burman et al., *Appl. Phys. Lett.*, 2008, 93193118, 1–3, © the American Institute of Physics, reproduced by permission.<sup>12</sup>

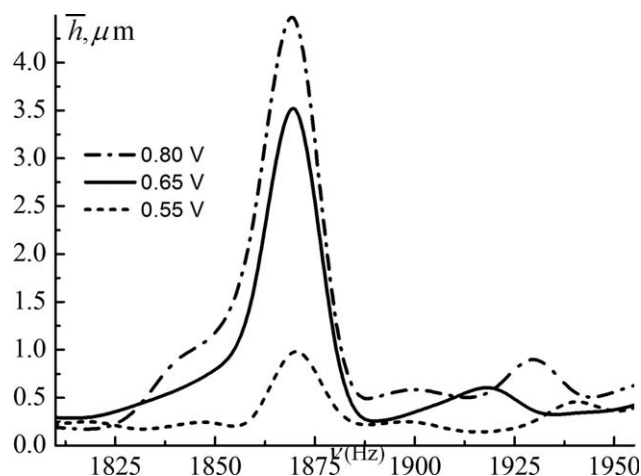


**FIGURE 19** Typical plots of ball flight heights,  $\bar{h}$ , versus input signal frequency,  $\nu = \Omega/2\pi$ , for different input signal amplitudes. From Burman et al., *Appl. Phys. Lett.*, 2008, 93193118, 1–3, © the American Institute of Physics, reproduced by permission.<sup>12</sup>

The elastic moduli of the as-spun nylon 6,6 nanofibers (see Fig. 15) was measured using the tensile and resonant vibration tests.<sup>12</sup> In the resonant vibration test, the tethered sample nanofiber with a bob at its tips can be considered as a string pendulum [see Fig. 18(a)], experiencing regular oscillations under the elastic force [see Fig. 18(c)], along with free flight only under gravity, which can be easily tracked [see Fig. 18(d)]. The resonant frequency of such a string pendulum, as recorded with an optical microscope, allows for determination the Young's modulus of the nanofiber (see Fig. 19). Using these methods, the dependence of the elastic modulus on the mode of deformation can be defined.

### Thermodynamic Properties of Polymer Nanofibers

Certain thermodynamic properties of nano-objects also demonstrate size-dependent behavior. For example, the temperature

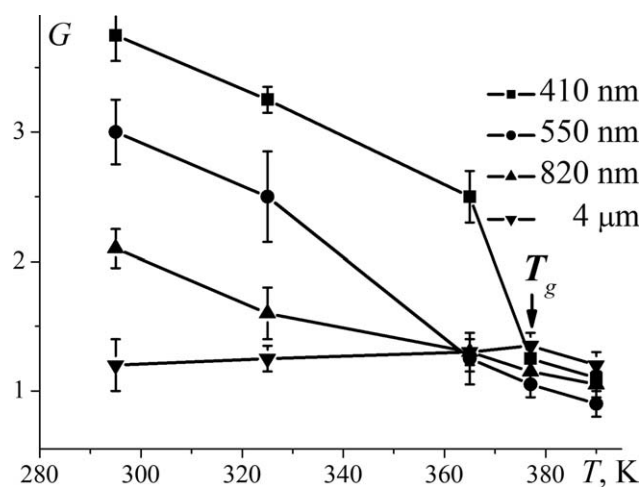


**FIGURE 20** Relative shear modulus,  $G$  of electrospun polystyrene fibers as a function of the temperature, at different fiber diameters. From Ji et al., *Langmuir*, 2006, 22, 1321–1328, © the American Chemical Society, reproduced by permission.<sup>27</sup>

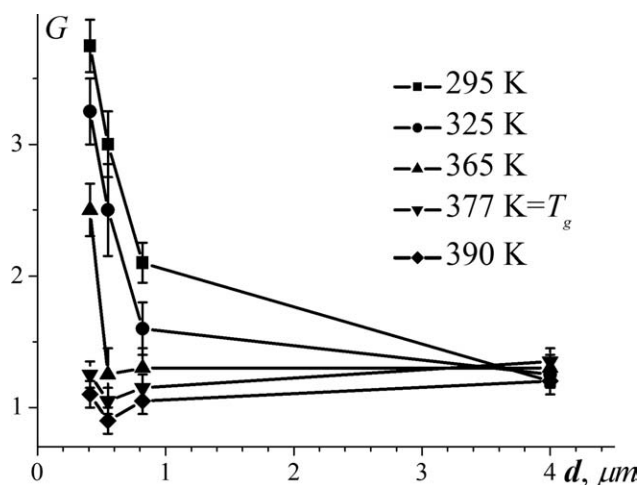


**FIGURE 21** Relative shear modulus,  $G$  of electrospun polystyrene fibers as a function of fiber diameters,  $d$ , at different temperatures, based on the data presented in Figure 20.

dependence of elastic modulus has been presented by Ji et al.<sup>27</sup> (see Fig. 20) and has been shown to differ for fibers of small versus large diameters at temperatures below their glass-transition temperature ( $T_g$ ). The elastic modulus of fibers of 4  $\mu\text{m}$  in diameter increases with elevating temperatures, corresponding with rubber elasticity, whereas it decreases for fiber diameters  $<1 \mu\text{m}$ , behavior common to solid and crystalline materials.

The observed dependence can be attributed to the influence of fiber diameter on entropy. Indeed, only negligible contribution of the entropy to elasticity of crystalline or amorphous materials at temperatures below  $T_g$  is seen, thereby leading to decreased elasticity with increasing temperatures. The negative slope in elasticity-temperature dependence can be explained by the dominant role of intermolecular interactions in thin nanofibers of diameters below 1  $\mu\text{m}$ . However, in thick nanofibers, where a positive dependence slope is observed, the role of entropy is dominant but constantly suppressed by decreasing fiber diameters.

The same data, presented in another form, demonstrate that modulus dependences on fiber diameter are modified as temperatures increase; at room temperature, elastic modulus monotonically increases as diameters decrease, and at temperatures above  $T_g$ , the dependence becomes nonmonotonic (see Fig. 21).

Many researchers have reported shifts in  $T_g$  for polymer nano-objects, a phenomenon summarized in a review paper authored by McKenna.<sup>65</sup> Both an increase and a decrease in  $T_g$  were observed. For example, Keddie et al.<sup>66</sup> showed that the glass transition temperature of thin polymer films is reduced, when compared with the bulk, by about 25 K for 100 Å. From these experiments, it might be concluded that the  $T_g$  shift does not depend on molecular weight for short polymers with a radius of gyration smaller than the film thickness, while the molecular-weight dependence is very important for larger polymers (leading to even larger  $T_g$

reductions) and then saturates at very large molecular weight.<sup>67</sup> On the other hand, experiments performed on strongly adsorbed films showed that the glass transition temperature increases in these cases by as much as 60 K for films 80-Å thick.<sup>68</sup>

In the case of nanoporous confinement, shifts in  $T_g$  can be attributed to surface interactions, or additional hydrostatic compression induced by the confinement, and not to size itself. Furthermore, the direction of the change in  $T_g$  can be simply controlled by tuning the strength of interfacial interactions and the dynamics of the confining medium. However, for nano-objects situated inside nanopores or nanochannels, or nanofilms lying on a substrate, interfacial interactions cannot be tuned. However, in nanofibers interfacial interactions do not impact the polymer matrix state and their unique properties can all be attributed to confinement.

Various explanations of the  $T_g$  shift, unrelated to interfacial interactions, have been proposed, including, decrease in film density,<sup>69</sup> decrease in entanglement density,<sup>70</sup> and increase in chain-end concentration near the surface.<sup>71–73</sup> All of these theories consider object geometrics only and can be responsible for  $T_g$  shifts much smaller than those experimentally registered. In parallel, de Gennes<sup>17</sup> proposed the effect of collective motions along the “loop” near the surface (in place of a chain) as responsible for polymerization index decreases. However, such effects only occur in the near-surface layer, which has a thickness close to the radius of gyration of the polymer coil,  $R_g$ . Thus, these suggested models lead to shifts on scales that do not coincide with the experimentally observed magnitude of change and therefore require further analysis.

### Shift in Melting Temperature of Semicrystalline Polymer Nanofibers

Recent experimental results have shown a decrease in the melting temperature of electrospun nanofibers as their

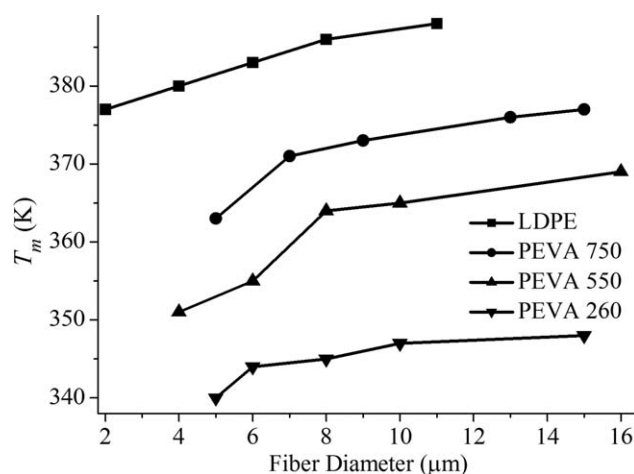


**FIGURE 22** Melting temperature versus diameter of nanofibers. The melting temperatures of the nanofibers were obtained using shear modulation force microscopy (SMFM). The melting temperature of the thickest fibers for each polymer coincided with the bulk melting temperature obtained using DSC.<sup>42</sup>

diameters decrease (see Fig. 22). Similar behavior was obtained by Liu et al.<sup>16</sup> for poly(ethylene-co-vinyl acetate) (PEVA) fibers with embedded clay and by Wang and Barber<sup>15</sup> for polyethylene oxide (PEO) fibers. This phenomenon was explained by adapting the Gibbs–Thompson equation, which is commonly used to describe the shift in the melting temperature of monocrystals, lamellas, or spherulites, having a scale of  $\sim 10$  nm.<sup>18</sup> However, applicability of the Gibbs–Thompson model to polymer microfiber behavior remains questionable, as the observed shift in melting temperature in electrospun fibers exceeded those of the crystalline structures by two orders of magnitude.

To explain the size-dependent melting temperature recorded for nanofibers, it was assumed that the influence of the fabrication stage of as-spun polymer nanofibers had a crucial impact on their final thermodynamic properties, resulting from the nonequilibrium thermodynamic state of the polymer matrix during electrospinning. At the same time, crystallization and/or spherulite formation<sup>16</sup> neither allow for relaxation in the amorphous interlayers between crystals nor for relaxation within the spherulites themselves, due to the presence of tie molecules. The nonequilibrium state of these amorphous interlayers can account for the observed shift in the melting temperature of semicrystalline nanofibers.

The temperature of the melting phase transition is related to jumps in energy and entropy as follows:

$$T_{\text{melt}}^{\text{fiber}} = \frac{\Delta E}{\Delta S} = \frac{Q}{\Delta S_{\text{bulk}} + \delta S_{\text{fiber}}} \quad (13)$$

where  $Q = \Delta E$  is the specific melting heat, and the additional jump in entropy,  $\delta S_{\text{fiber}}$ , is related to the internal structure of the fiber in the polymer matrix that results in the observed shift in the melting temperature.

The internal structure of a semicrystalline electrospun polymer nanofiber is characterized by highly oriented polymer crystals and amorphous portions of the polymer matrix, when compared with bulk.<sup>11</sup> At first glance, one may attribute the additional jump in entropy to polymer crystal orientation, which results in a decrease of the overall entropy of the fiber below the melting temperature. However, this assumption turned out to be wrong as the melting temperature of ordinary (macro-) fibers is no different than that of bulk, despite prominent crystal orientation in macrofibers. It would seem that crystal orientation does not affect the melting temperature, as the crystals within the fibers are isolated and do not interact with one another.

The influence of the amorphous portion of the polymer matrix on the state of polymer crystals is very complicated. Because of the relatively large interface of nanofiber microcrystals, the amorphous portions of a polymer matrix may significantly affect the crystal state. However, no shift in melting temperatures is observed in ordinary thick fibers, where similar degrees of microcrystal interfaces also exist. Thus, it can be concluded that the nanocrystal interface plays no significant role in this phenomenon. Therefore, a variation in interface area, resulting from variations in inner fiber

crystal sizes, which could be dependent on the fiber diameter, does not affect the melting temperature.

The level of chain entanglement, the single structural parameter differentiating between nanofibers and thick fibers, may be responsible for these observed temperature shifts. The initial fabrication conditions dictate the polymer matrix state for bulk and thick fibers, as well as for nanofibers. Nanofibers are formed under rapid solvent evaporation conditions, resulting in the fixation of macromolecule entanglements corresponding to the initial concentration of the semidilute polymer solution used in the electrospinning process. This topological network is not capable of relaxing and establishes an equilibrium state due to tie chains incorporated between two (or more) crystals. Indeed, fixation of a chain end results in fixed topology of the polymer matrix, where changes are only possible when a chain end becomes free, which only occurs during melting. On crystal melting, topological knot concentrations increase. The entropy corresponding to the network of topological knots also increases, as defined by  $\delta S_{\text{fiber}}$ .

The physical basis of the above mechanism can be explained in terms of tie molecules, which attempt to leave the crystal to allow for an increase in the degree of entanglement, thereby weakening the crystal and promoting its destruction. As a result, crystal melting requires less energy and occurs at a lower temperature. Thermodynamically, one can say that the low degree of chain entanglement in the amorphous portion of the polymer matrix does not permit equilibrium packing, and the system tends to become dense. As a result, any negative additive to the interface pressure between amorphous and crystal polymer portions induces a decrease in the melting temperature.

When estimating the additive in entropy jump,  $\delta S_{\text{fiber}}$ , as a function of fiber diameter, assuming similarity of the system of topological knots to a gas, the entropy for one knot is equal to the logarithm of its concentration,  $\ln(c_{\text{kn}})$ . The knot concentration is less than the polymer concentration by  $n_{\text{kn}}$  times, where  $n_{\text{kn}}$  is the mean number of monomers between two neighboring knots along the contour of the polymer chain. Therefore, the additive in entropy jump,  $\delta S_{\text{fiber}}$ , can be defined as:

$$\delta S_{\text{fiber}} = \ln(n_{\text{kn}}^{\text{solv}}/n_{\text{kn}}^{\text{bulk}}) \quad (14)$$

The knot concentration,  $n_{\text{kn}}^{\text{solv}}$ , is determined by the solvent concentration used in the electrospinning process, according to:<sup>42</sup>

$$n_{\text{kn}}^{\text{solv}} = (\phi_{\text{solv}}/\phi^*)^{\frac{1}{1-3v}} N \quad (15)$$

where  $\phi_{\text{solv}}$  is the volumetric concentration of the solvent used in the electrospinning process,  $\phi^* = N^{1-3v}$  is the volumetric crossover concentration corresponding to the polymer chain overlap, and  $N$  is the degree of polymerization.

The diameter of as-spun nanofibers is dependent on the initial concentration,  $\phi_{\text{solv}}$ , of the spinning polymer solution. This experimental pattern can be best described with the help of the following empirical scaling equation:<sup>29</sup>

$$\frac{d_{\text{fiber}}}{d_0} = (\phi_{\text{solv}}/\phi^*)^\alpha = (c_{\text{solv}}/c^*)^\alpha, \quad (16)$$

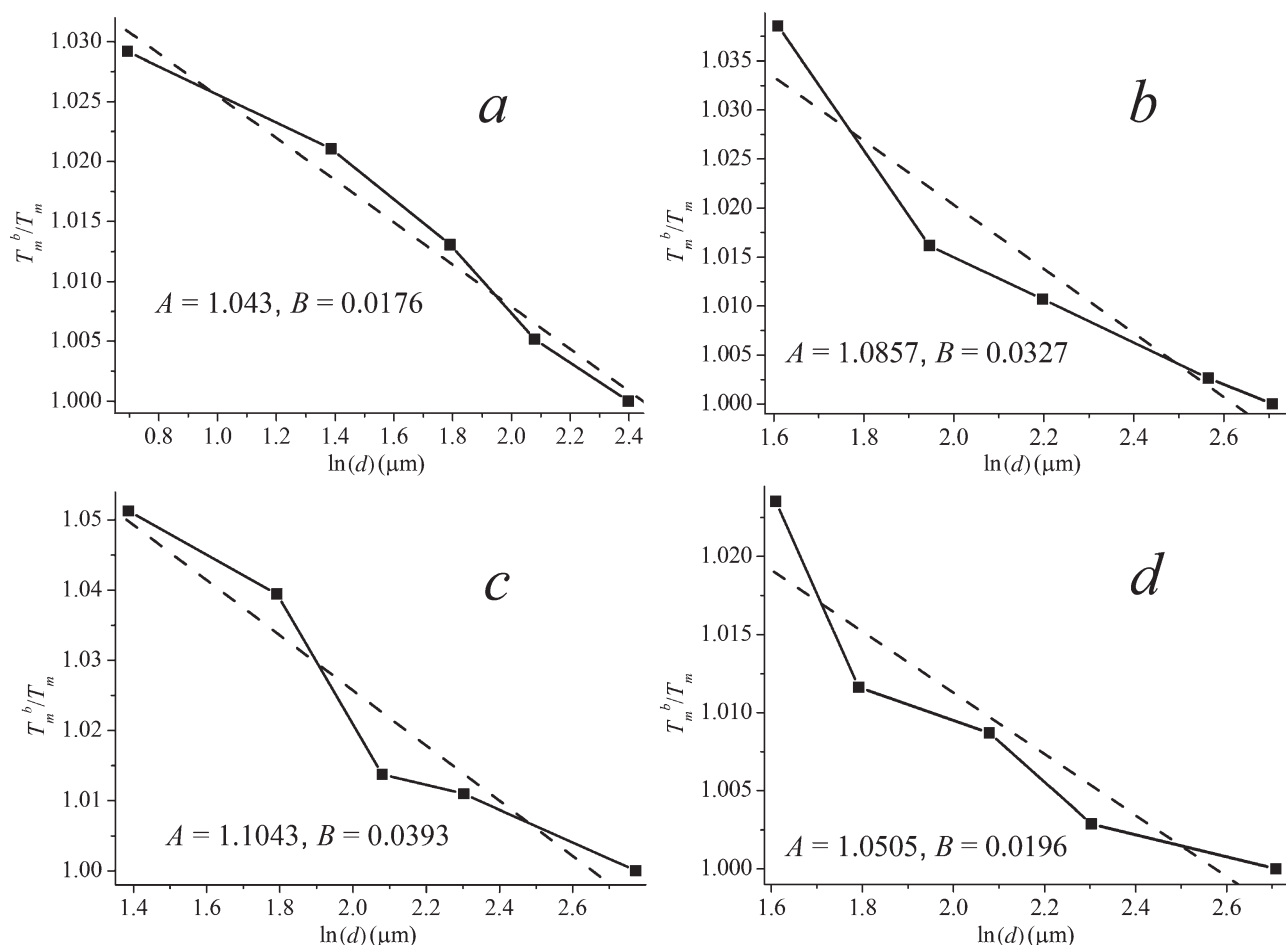


**FIGURE 23** Fitting of experimental values of melting temperatures versus  $\ln(d)$ , using linear eq 18, for as-spun nanofibers of LDPE (a), PEVA750 (b), PEVA550 (c), and PEVA 260 (d).<sup>42</sup>

where  $\alpha = 2.99$ , and  $d_0 = 0.11 \mu\text{m}$ ;<sup>16</sup>  $c_{\text{solv}}$  and  $c^*$  are the corresponding weight concentrations.

When substituting eqs 15 and 16 into eq 14, we reach the final equation for the additive in entropy jump,  $\delta S_{\text{fiber}}$ , as a function of fiber diameter:

$$\begin{aligned} \delta S_{\text{fiber}} &= \ln \left[ \frac{N}{n_{\text{kn}}^{\text{bulk}}} \left( \frac{d_0}{d_{\text{fiber}}} \right)^{\frac{1}{\alpha(3v-1)}} \right] \\ &= 0.67 \left[ \ln \left( \frac{Nd_0}{n_{\text{kn}}^{\text{bulk}}} \right) - \ln(d_{\text{fiber}}) \right] \end{aligned} \quad (17)$$

where  $v = 0.5$ .

Using eq 17, the melting temperature of as-spun nanofibers can be expressed as a function of fiber diameter and written as a linear function of  $\ln(d_{\text{fiber}})$ :

$$\frac{T_{\text{melt}}^{\text{bulk}}}{T_{\text{melt}}^{\text{fiber}}} = 1 + \frac{T_{\text{melt}}^{\text{bulk}}}{Q} \delta S_{\text{fiber}} = A - B \ln(d_{\text{fiber}}) \quad (18)$$

where  $A = 1 + (T_{\text{melt}}^{\text{bulk}}/Q) \ln(Nd_0^{0.67}/n_{\text{kn}}^{\text{bulk}})$ ,  $B = 0.67T_{\text{melt}}^{\text{bulk}}/Q$ , and  $T_{\text{melt}}^{\text{bulk}} = Q/\Delta S_{\text{bulk}}$  is the melting temperature of the bulk.

The order of magnitude of the parameters contained in eq 18 can be estimated by the example of polyethylene (PE;

specific melting heat = 71 J/g; molecular weight of its monomer = 28), whose properties are somewhat similar to those of the materials tested above. To estimate the specific melting heat,  $Q$ , which corresponds to the part of polymer chain between two neighboring topological knots, the loop consisting of  $n_{\text{kn}}^{\text{bulk}} \approx 10^2$  monomers, must be considered. Therefore,  $Q = 71 \times 28 \times 10^2 \approx 2 \times 10^5$  J/mol and  $B = 0.67RT_{\text{melt}}^{\text{bulk}}/[K]/Q \approx 0.011$  ( $R = 8.314$  J/mol·K). Assuming that  $N \approx 10^4$ , corresponding to the typical degree of PE polymerization, we obtain  $A = 1 + (RT_{\text{melt}}^{\text{bulk}}[K]/Q) \ln(Nd_0^{0.67}/n_{\text{kn}}^{\text{bulk}}) \approx 1.05$ .

Figure 23 presents experimental data fitting to the obtained linear dependence outlined in eq 18 and demonstrates that both the theoretical dependence and the above numerical estimations are in good agreement with the experimental data.

#### PHYSICAL INTERPRETATION OF NANOFIBER MECHANICAL PROPERTIES

The observed size-dependent features of polymer nanofibers are poorly understood, and lack of explanation, using mechanical (macroscopic) dogmas, requires further examination of the systems in question. In the following sections, we first present a mechanical interpretation for the size-dependent



nanofiber behavior, relying solely on surface tension effect, then review existing computational models incorporating surface energy into continuum mechanics, and finally provide microscopic interpretation of mechanical nanofiber properties based on their supermolecular structure.

### Mechanical Interpretation Based on Influence of Surface Tension

Nanofiber size-dependent behavior has often been attributed to surface effects.<sup>74,75</sup> Cuenot et al.<sup>9,74</sup> interpreted abrupt increase in the Young's modulus of nano-objects by using the "nano-object = bulk + surface" ansatz. This approach was based on the fact that the total energy,  $U$ , of a deformed nanofiber or nanotube includes the surface energy, which results in an increase of Young's modulus for small diameters. Thus, assuming a force,  $F$ , applied at the beam midpoint and inducing a deflection,  $\delta$ , an expression for the total energy,  $U$ , of the bent beam is:

$$U = -F\delta + \frac{1}{2}k_t\delta^2 + (1-\nu)\gamma\Phi\Delta L. \quad (19)$$

where  $k_t$  is the beam elastic stiffness,  $\Phi$  is the contour length of its section,  $\Delta L$  is the length variation,  $\nu$  is the Poisson's ratio, and  $\gamma$  is the surface tension of the material. For these clamped conditions, the elastic stiffness can be calculated as:

$$k_t = \frac{192EI}{L^3}, \quad (20)$$

where  $E$  is the Young's modulus and  $I$  is the moment of inertia of the section.

In eq 19, the first term denotes the work of the applied force, the second term represents the elastic deformation energy of the bent beam, and the third term corresponds to the deformation energy of the surface resulting from beam extension. Beam bending, when both nanofiber/tube ends are clamped, preventing longitudinal end displacement, results in extension of nanotube length and, hence, in an increase of the surface area. The energy term dealing with the surface increase, accounts for material compressibility,  $\nu$ .

For slight bending, the extension of the bent beam is given by:

$$\Delta L = \frac{1}{2} \int_0^L y'(x)^2 dx, \quad (21)$$

where  $y(x)$  is the deflection curve of the beam with a concentrated load applied at the midpoint of the suspended length (in eq 21 the approximation  $\sqrt{1+\varepsilon} - 1 \approx 0.5\varepsilon$  was used).

Because of nonlinearity, the surface deformation energy term demonstrates quadratic dependence on the central deflection, giving rise to an additive surface contribution to beam stiffness. As a first approximation, it is assumed that the usual deflection curve of a clamped beam is not affected by the surface tension contribution. Thus, for clamped boundary conditions, the beam extension can be easily calculated and expressed as:

$$\Delta L = \frac{12\delta^2}{5L}, \quad (22)$$

When substituting eq 22 into eq 21, the following expression for the total energy of the bent beam is obtained:

$$U = -F\delta + \frac{1}{2}(k_t + k_s)\delta^2, \quad (23)$$

where  $k_s = 24(1-\nu)\gamma\Phi/5L$ .

For the bent beam,  $\Phi = \pi d$  and  $I = \pi d^4/64$ , where  $d$  is the diameter of the bent beam. Therefore, the effective stiffness coefficient is  $k_t + k_s$ , and the effective Young's modulus can be renormalized as follows:

$$E_{\text{eff}} = E + \frac{8(1-\nu)\gamma L^2}{5d^3}, \quad (24)$$

and, according to Cuenot et al.,<sup>74</sup> this dependence lies in agreement with the experimental data shown in Figure 13.

Although the above speculations seem well-founded and seemingly describe the influence of surface mechanical properties of materials of reduced size, a detailed analysis highlights the dependence of this effect on the mode of deformation. Indeed, in the case of "uniaxial" stretching of a fiber,<sup>76</sup> the density of elastic energy is a quadratic function of reduced elongation,  $\Delta l/l$ , whereas the density of additional surface energy, in case of simplest approximation, is a "linear" function:

$$U_{el} = \frac{E}{2}(\Delta l/l)^2, \quad U_{sf} = \frac{2\gamma}{r}(\Delta l/l), \quad (25)$$

where  $\gamma$  is the surface tension coefficient of a polymer, and  $r$  is the fiber radius.

The stress caused by the elastic force is proportional to the fiber elongation, as expressed through Young's modulus,  $E$ , the slope of this dependency relationship. In parallel, the stress caused by forces of surface tension does not depend on elongation and has no effect on the fiber's Young's modulus.

More exact estimation considering volume conservation of a deformed fiber, results in the same linear dependence of  $U_{sf}$ , in which the coefficient is renormalized. Indeed, volume conservation of a deformed fiber,  $V = \pi r^2 l = \tilde{V} = \pi \tilde{r}^2(l + \Delta l)$ , results in a decrease of its radius:

$$\tilde{r} = \frac{r}{\sqrt{1 + \Delta l/l}}. \quad (26)$$

The increase of fiber surface is expressed as:

$$\Delta S = \tilde{S} - S = 2\pi \tilde{r}(l + \Delta l) - 2\pi r l = S \left( \sqrt{1 + \Delta l/l} - 1 \right) \approx S \frac{\Delta l}{2l}, \quad (27)$$

and the density of additional surface energy remains a linear function:

$$\tilde{U}_{sf} = \frac{\gamma}{r}(\Delta l/l), \quad (28)$$

Therefore, although surface tension forces are of great importance to nanoscale object behavior, they cannot be held responsible for the increases in Young's modulus observed in

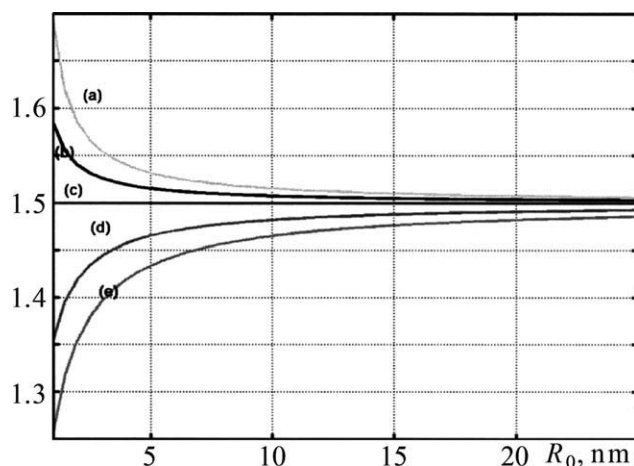


**FIGURE 24** Stress concentration as a function of surface properties and void radius. (a) Solution with surface modulus =  $2K_s$ , Al [1,0,0]; (b) solution with surface modulus = nominal  $K_s$  for Al [1,0,0]; (c) classical solution without surface effects, that is,  $K_s = 0$ ; (d) solution with surface modulus =  $2K_s$  Al [1,1,1]; (e) solution with surface modulus = nominal  $K_s$ , Al [1,1,1]. From Sharma et al., Appl. Phys. Lett., 2003, 82, 535–537, © the American Institute of Physics, reproduced by permission.<sup>61</sup>

tensile tests of nanofibers, where the increase in fiber surface area is proportional to its elongation.<sup>9</sup>

### Surface Influence on the Elastic Properties of Nanoobjects

Theoretical models incorporating the free surface energy into the continuum theory of mechanics have been suggested<sup>61,75</sup> for explaining the size-dependent elastic behavior of the nano-scale objects (i.e., particles, wires, and films). In traditional continuum mechanics, such surface free surface energy is typically neglected, as it is associated with only a few layers of atoms near the surface, which occupy a minor percentage of the total volume of material of interest. However, due to the increasing surface-to-volume ratio of nanosized particles, surface effects become more significant and impact material properties in a size-dependent manner. Namely, due to surface stresses, the self-equilibrium state of such a particle differs from the perfect crystal lattice of an infinite extent, resulting in an altered effective modulus among nanoelements.

Thus, Sharma et al.<sup>61</sup> calculated the stress concentration of a spherical aluminum cavity under hydrostatic tension, as a function of the cavity radius  $R_0$  (see Fig. 24). An increase or decrease in the stress concentration depends on the sign of the surface elastic constant,  $K_s > 0$ . The surface-dictated effects cause the stress concentration to decrease with decreasing pore size when  $K_s > 0$ , or alternatively, to increase at  $K_s < 0$ . The classical case, void of surface effects, corresponds to  $K_s = 0$  and is, as expected, is independent of pore size. Note that the scale of the stress alteration amounts only to 5 nm!

Dingreville et al.<sup>75</sup> showed that due to surface stresses, the nanospecimen is nonhomogeneous when in its equilibrium state. When materials are not homogeneous, as in the case of composite materials, their elastic moduli may vary from

point to point, supporting the concept of effective modulus. Based on this approach, effective Young's modulus,  $E$ , was calculated (see Fig. 25) for Cu films and wires of varying sizes. Note that in these calculations, the scale of the modulus alteration also does not exceed 5 nm!

Thus, one can conclude that the surface effects alone cannot quantitatively account for the above phenomenon. Moreover, in contrast to the commonly held view that surface effects are dominant, we suggest that the internal microstructure of polymer nanofibers plays a more dominant role in the deformation process than previously thought. Xu et al. reached the same conclusion regarding ultrathin crosslinked polymer films.<sup>77</sup> These authors argue that the surface tension contribution is insufficient to fully account for the overall rubbery stiffening behavior observed, which, they propose, should be attributed to a mixture of both molecular (or confinement-induced) stiffening and surface tension effects.

In our opinion, the suggested confinement-induced phenomenon assumes a dominant role in polymer nanofiber reinforcement, while the effect of surface tension is negligible. Nevertheless, it has only been indirectly proven that the size-dependent behavior of nano-objects is not related to surface energy. Only direct experimental measurement of surface energy influence will be able to fully address questions relating to correlations between surface effects and abrupt increases in Young's modulus, as well as the thermodynamic property modifications in polymer nanofibers.

### Microscopic Interpretation Based on Supermolecular Structure of Polymer Nanofibers

One may be tempted to attribute increased elasticity to a gradual ordering of the nanofiber microstructure as a function of the diameter. This can indeed be the case when structure parameters such as degree of crystallinity, orientation of crystallites along the fiber axis, and orientation of macromolecules of the amorphous fiber regions are noticeably higher

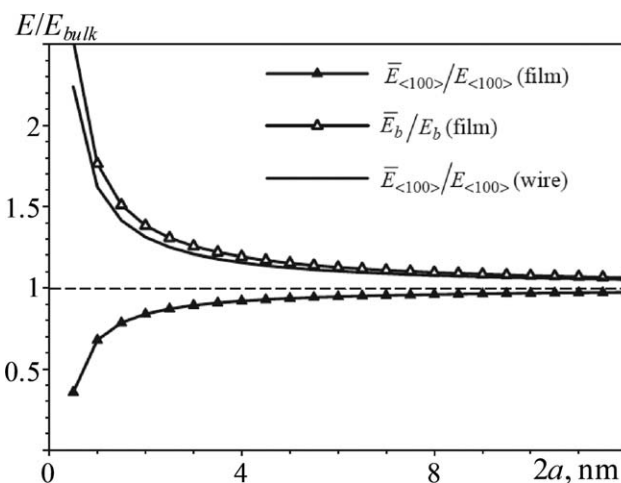


**FIGURE 25** Normalized effective Young's modulus,  $E$ , of Cu films and wires of various sizes. From Dingreville et al., J. Mech. Phys. Solids, 2005, 53, 1827–1854, © Elsevier, reproduced by permission.<sup>75</sup>

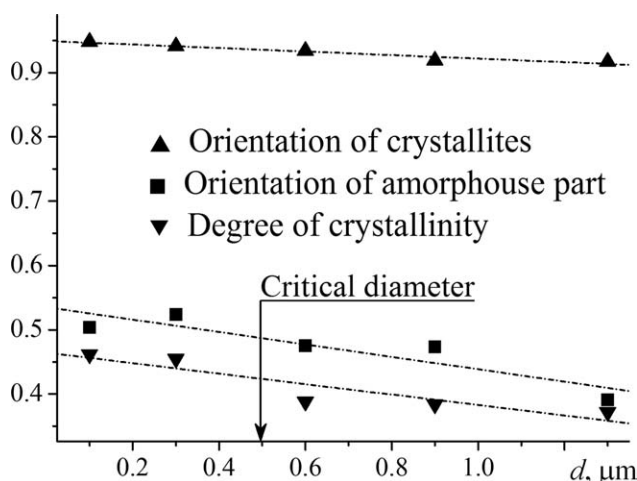


**FIGURE 26** X-ray analysis of nanofiber structural properties as a function of its diameter. Degree of crystallite orientation along the fiber axis, degree of crystallinity, and order parameter of macromolecule orientation in the amorphous regions of the fiber versus fiber diameter,  $d$  of electrospun nylon 6,6 nanofibers. From Arinstein et al., Nat. Nanotechnol., 2007, 2, 59–62, © Nature Nanotechnology, reproduced by permission.<sup>11</sup>

as a result of processing of nanofibers with diameters less than a determined critical value.

Structural properties of nanofibers featuring average diameters of 100, 300, 600, 900, and 1300 nm have been studied using both wide-angle X-ray (WAXS) scattering and small-angle X-ray scattering. However, the experimental results did not demonstrate any abrupt diameter-dependent changes in nanofiber microstructure. X-ray analysis demonstrated only a mild, monotonous increase in nanofiber crystallinity and orientation, as a function of their diameters (see Fig. 26). Thus, this weak correlation cannot be responsible for the dramatic change in the Young's modulus.

In addition, the average crystallite size ( $\sim 4$  nm) does not depend on nanofiber diameter and is significantly smaller than the average fiber diameter. Therefore, as the crystallinity remains almost constant with decreasing in nanofiber diameter, no significant change is expected for the crystallite percolation structure arising from tie chains interconnecting adjacent crystals.

Thus, analysis of the global state parameters of the polymer matrix of the electrospun nanofibers can not explain the observed size-dependent phenomena. Therefore, an alternative explanation for the physical mechanism underlying the abrupt increase in nanofiber elastic modulus is required. We began by examination of a higher level of the nanofiber local microstructure, namely the supermolecular structure of the amorphous nanofiber portion. Indeed, in elongation experiments, polymer stretching (i.e., their orientational ordering) led to a significant increase the fiber's Young's modulus, without affecting polymer matrix crystallinity. Therefore, further attention was placed on the amorphous portion of the fiber polymer matrix, namely on the supermolecular nanofiber structures containing oriented portions of polymer chains. As

systems of semiflexible polymers, especially within polymer fibers, contain regions of oriented macromolecules (or of their parts), we proceeded with the assumption that such supermolecular structures could be responsible for the abrupt increase in the elastic modulus of nanofibers. As no dramatic structural modifications were observed experimentally, focus was on tracing possible dimensional effects. To this end, key questions were raised with regards to the required size of the oriented regions in relation to the nanofiber diameter (see Fig. 27) to dictate the proposed elasticity-microstructure relationship.

Multiple factors, such as physicochemical properties of macromolecules, formation conditions, and postprocessing, influence the supermolecular structures of polymer fibers, complicating their size estimations. However, given the fact that the orientational ordering of chains in polymer fibers is not lower than in polymer melt, estimation of the orientation correlation length in polymer melt can provide us with a lower bound of the required supermolecular structure size. Such estimations have already been performed for liquid oligomer systems in analysis of the non-Gaussian conformational statistics of relatively short macromolecules,<sup>78–80</sup> using scaling concepts in polymer physics.<sup>48</sup>

It is well established that the volume,  $V_{ch} \propto a^3 N^{3\nu}$ , occupied by a polymer chain, consisting of  $N$  links of size  $a$ , considerably exceeds the total volume of all chain monomers. This volume, which is occupied by the trial chain, contains many polymer chains. According to the ergodicity hypothesis, all of these chains pass through the total volume,  $V_K = V_{ch}/(N/n_K) \propto a^3 n_K^{3(1-\nu)+1} N^{3\nu-1}$ , corresponding to a single Kuhn segment consisting of  $n_K$  links. The volume,  $V_K$ , is filled with rods of length  $l_K = a n_K$  and diameter  $a$ , which are the Kuhn segments of other chains. The nondimensional density of these rods is defined as  $C \propto \theta/(a^3 n_K)$ , where  $\theta$  is a specific volume of polymer with a value approaching one unit,  $\theta \sim 1$ .

As the Kuhn segments of different chains are statistically independent, the above system is equivalent to the well-known system of rigid rods. Therefore, the Onsager<sup>81</sup> model can be adopted for the present analysis of orientational ordering of Kuhn segments. Such orientational ordering occurs at Kuhn

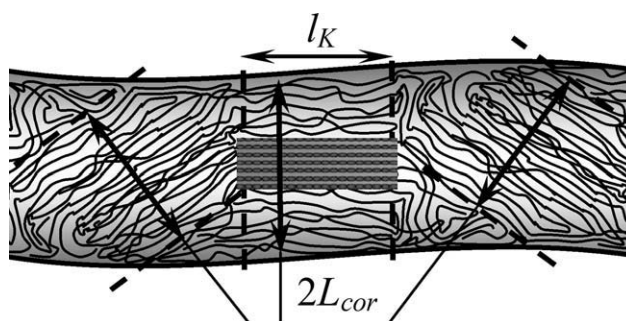


**FIGURE 27** A sketch of the arrangement of crystallites and surrounded oriented amorphous matrix in polymer nanofiber, where,  $L_{cor}$  is the orientation correlation length within the amorphous polymer portion, and  $l_K$  is the length of the Kuhn segment. From Arinstein et al., Nat. Nanotechnol., 2007, 2, 59–62, © Nature Nanotechnology, reproduced by permission.<sup>11</sup>



segment concentrations exceeding the critical value,  $C_{cr} \propto 1/(a l_K^2) = 1/(a^3 n_K^2)$ , corresponding to that of a specific volume,  $\theta_{cr} \propto 1/n_K$ . As the current analysis relates to polymers with relatively long Kuhn segments, the system concentration is much higher than the critical one, allowing for orientational ordering to take place. The correlation length in such ordered systems is of particular interest, as it corresponds to the size of the supermolecular structures in question.

The desired correlation length can be calculated based on the modified Onsager model, which corresponds to the case of high rod density:<sup>78,80</sup>

$$L_{cor} \propto \frac{a}{\sqrt{\theta}} [n_K \ln(1 - \theta)]^2. \quad (29)$$

Given the values of the correlation length and of the free volume in polymer systems,  $\vartheta = 1 - \theta$ , we can estimate the size of oriented regions in the polymer nanofibers. The free volume in polymer systems can vary considerably, as seen in the amorphous phase, where  $\vartheta$  can amount to ~20% but can decrease to ~2% in crystallites.<sup>82</sup> Assuming a free volume of  $\vartheta \approx 0.08$  (the arithmetic mean of the highest and lowest estimated values of the free volume described in Ref. 82),  $a \approx 0.1$  nm, and  $n_K \approx 15$ , the cross-section size of the ordered region is:

$$D = 2L_{cor} \propto \frac{2a}{\sqrt{\vartheta}} [n_K \ln(\vartheta)]^2 = \frac{2 \cdot 0.1 \cdot [15 \ln(0.08)]^2}{\sqrt{0.92}} \approx 300 \text{ nm} \quad (30)$$

This size amounts to a bit more than half of the fiber diameter, at which point an abrupt increase in the fiber's modulus is observed. Nevertheless, this estimation can be viewed as a satisfactory value.

One can improve the suggested estimation by considering additional factors influencing the formation of supermolecular structures in nanofibers. More specifically, surface tension creates additional radial pressure within the fibers, resulting in contraction of the polymer matrix, thereby inducing a decrease in the free volume of the nanofiber and an increase in its specific volume. However, surface tension has a negligible effect on the correlation length of the amorphous portion of a polymer matrix, and therefore, surface effects cannot explain the observed increase in the Young's modulus of nanofibers.

## CONCLUSIONS

The goal of the present work was to provide an overview of the scientific challenges presented by the exceptional mechanical properties and unique thermodynamic behavior of polymer nanofibers. Briefly, our conclusions can be formulated as follows:

- The state of polymer matrix within electrospun nanofibers is nonequilibrium. This nonequilibrium arises from polymer molecule stretching, which occurs during the electrospinning process. This stretched state of polymer matrix can partially relax during final solvent evaporation.
- Supermolecular structures arising in nanofiber polymer matrices provide an additional scale, which must be considered, when analyzing nano-objects properties.

- Confinement of these supermolecular structures, caused by the shrinking of the transversal size of polymer nanofibers, plays a dominant role in modification the mechanical and thermodynamic properties of nanofibers.

When considering the fact that the processing conditions do affect the final state of the polymer matrix of nanofibers, the possibility to generalize the above ideas to other nano-objects will require additional analyses.

## ACKNOWLEDGMENTS

This work was partly supported by the BSF, United States, Israel Bi-National Science Foundation (grant 2006061), and the RBNI—Russell Berrie Nanotechnology Institute at the Technion—I.I.T. AA acknowledges support from the Kamea Program, Israel Ministry of Absorption.

## REFERENCES AND NOTES

- 1 Reneker, D. H.; Yarin, A. L.; Zussman, E.; Xu, H. *Adv. Appl. Mech.* **2007**, *41*, 43–195.
- 2 Thavasi, V.; Singh, G.; Ramakrishna, S. *Energy Environ. Sci.* **2008**, *1*, 205–221.
- 3 Wu, H.; Zhang, R.; Sun, Y.; Lin, D. D.; Sun, Z. Q.; Pan, W.; Downs, P. *Soft Matter* **2008**, *4*, 2429–2433.
- 4 Baker, S. C.; Atkin, N.; Gunning, P. A.; Granville, N.; Wilson, K.; Wilson, D.; Southgate, J. *Biomaterials* **2006**, *27*, 3136–3146.
- 5 Maretschek, S.; Greiner, A.; Kissel, T. J. *Controlled Release* **2008**, *127*, 180–187.
- 6 Ra, E. J.; An, K. H.; Kim, K. K.; Jeong, S. Y.; Lee, Y. H. *Chem. Phys. Lett.* **2005**, *413*, 188–193.
- 7 Greiner, A.; Wendorff, J. H. *Angew. Chem. Int. Ed.* **2007**, *46*, 5670–5703.
- 8 Chang, C. C.; Huang, C. M.; Chang, Y. H.; Kuo, C. S. *Opt. Express* **2010**, *18*, A174–A184.
- 9 Cuenot, S.; Demoustier-Champagne, S.; Nysten, B. *Phys. Rev. Lett.* **2000**, *85*, 1690–1693.
- 10 Tan, E. P. S.; Goh, C. N.; Sow, C. H.; Lim, C. T. *Appl. Phys. Lett.* **2005**, 86073115, 1–3.
- 11 Arinstein, A.; Burman, M.; Gendelman, O.; Zussman, E. *Nat. Nanotechnol.* **2007**, *2*, 59–62.
- 12 Burman, M.; Arinstein, A.; Zussman, E. *Appl. Phys. Lett.* **2008**, 93193118, 1–3.
- 13 Yuya, P. A.; Wen, Y. K.; Turner, J. A.; Dzenis, Y. A.; Li, Z. *Appl. Phys. Lett.* **2007**, 90111909, 1–3.
- 14 Shin, M. K.; Kim, S. I.; Kim, S. J.; Kim, S. K.; Lee, H.; Spinks, G. M. *Appl. Phys. Lett.* **2006**, *89*, 231929, 1–3.
- 15 Wang, W.; Barber, A. H. *Nanotechnology* **2010**, *21*, 225701, 1–9.
- 16 Liu, Y.; Li, C. H.; Chen, S.; Wachtel, E.; Koga, T.; Sokolov, J. C.; Rafailovich, M. H. J. *Polym. Sci. Part B: Polym. Phys.* **2009**, *47*, 2501–2508.
- 17 de Gennes, P. G. *Euro. Phys. J. E* **2000**, *2*, 201–203.
- 18 Alcoutlabi, M.; McKenna, G. B. J. *Phys. Condens. Matter* **2005**, *17*, R461–R524.
- 19 Wang, Y.; Rafailovich, M.; Sokolov, J.; Gersappe, D.; Araki, T.; Zou, Y.; Kilcoyne, A. D. L.; Ade, H.; Marom, G.; Lustiger, A. *Phys. Rev. Lett.* **2006**, *96*, 028303, 1–4.



- 20 Xavier, J. H.; Li, C.; Rafailovich, M. H.; Sokolov, J. *Langmuir* **2005**, *21*, 5069–5072.
- 21 Despotopoulou, M. M.; Frank, C. W.; Miller, R. D.; Rabolt, J. F. *Macromolecules* **1995**, *28*, 6687–6688.
- 22 Despotopoulou, M. M.; Frank, C. W.; Miller, R. D.; Rabolt, J. F. *Macromolecules* **1996**, *29*, 5797–5804.
- 23 Wang, H. P.; Keum, J. K.; Hiltner, A.; Baer, E. *Macromol. Rapid Commun.* **2010**, *31*, 356–361.
- 24 Krausch, G.; Dai, C. A.; Kramer, E. J.; Marko, J. F.; Bates, F. S. *Macromolecules* **1993**, *26*, 5566–5571.
- 25 Fasolka, M. J.; Banerjee, P.; Mayes, A. M.; Pickett, G.; Balazs, A. C. *Macromolecules* **2000**, *33*, 5702–5712.
- 26 Xiang, H. Q.; Shin, K.; Kim, T.; Moon, S.; McCarthy, T. J.; Russell, T. P. *J. Polym. Sci. Part B: Polym. Phys.* **2005**, *43*, 3377–3383.
- 27 Ji, Y.; Li, B. Q.; Ge, S. R.; Sokolov, J. C.; Rafailovich, M. H. *Langmuir* **2006**, *22*, 1321–1328.
- 28 Wong, S. C.; Baji, A.; Leng, S. W. *Polymer* **2008**, *49*, 4713–4722.
- 29 Gupta, P.; Elkins, C.; Long, T. E.; Wilkes, G. L. *Polymer* **2005**, *46*, 4799–4810.
- 30 Larrondo, L.; Manley, R. S. J. *J. Polym. Sci. Part B: Polym. Phys.* **1981**, *19*, 909–920.
- 31 Stephens, J. S.; Frisk, S.; Megelski, S.; Rabolt, J. F.; Chase, D. B. *Appl. Spectrosc.* **2001**, *55*, 1287–1290.
- 32 Hohman, M. M.; Shin, M.; Rutledge, G.; Brenner, M. P. *Phys. Fluids* **2001**, *13*, 2201–2220.
- 33 Shin, Y. M.; Hohman, M. M.; Brenner, M. P.; Rutledge, G. C. *Polymer* **2001**, *42*, 9955–9967.
- 34 Reneker, D. H.; Yarin, A. L.; Fong, H.; Koombhongse, S. J. *Appl. Phys.* **2000**, *87*, 4531–4547.
- 35 Megelski, S.; Stephens, J. S.; Chase, D. B.; Rabolt, J. F. *Macromolecules* **2002**, *35*, 3456–3466.
- 36 Guenther, A. J.; Khombhongse, S.; Liu, W.; Dayal, P.; Reneker, D. H.; Kyu, T. *Macromol. Theory Simul.* **2006**, *15*, 87–93.
- 37 Dayal, P.; Kyu, T. *Phys. Fluids* **2007**, *19*.
- 38 Dayal, P.; Liu, J.; Kumar, S.; Kyu, T. *Macromolecules* **2007**, *40*, 7689–7694.
- 39 Koombhongse, S.; Liu, W. X.; Reneker, D. H. *J. Polym. Sci. Part B: Polym. Phys.* **2001**, *39*, 2598–2606.
- 40 Casper, C. L.; Stephens, J. S.; Tassi, N. G.; Chase, D. B.; Rabolt, J. F. *Macromolecules* **2004**, *37*, 573–578.
- 41 Demir, M. M.; Yilgor, I.; Yilgor, E.; Erman, B. *Polymer* **2002**, *43*, 3303–3309.
- 42 Arinstein, A.; Liu, Y.; Rafailovich, M.; Zussman, E. *EPL* **2011**, *4*, 46001, 1–6.
- 43 Garcia, F. J.; Castellanos, A. *Phys. Fluids* **1994**, *6*, 2676–2689.
- 44 Reznik, S. N.; Zussman, E. *Phys. Rev. E* **2009**, *81*, 026313, 1–7.
- 45 Higuera, F. J. *J. Fluid Mech.* **2006**, *558*, 143–152.
- 46 Han, T.; Yarin, A. L.; Reneker, D. H. *Polymer* **2008**, *49*, 1651–1658.
- 47 Bellan, L. M.; Craighead, H. G.; Hinstroza, J. P. *J. Appl. Phys.* **2007**, *102*, 094308, 1–5.
- 48 de Gennes, P. G. *Scaling Concepts in Polymer Physics*; Cornell University Press: Ithaca, **1979**.
- 49 Pearson, D.; Herbolzheimer, E.; Grizzuti, N.; Marrucci, G. *J. Polym. Sci. Part B: Polym. Phys.* **1991**, *29*, 1589–1597.
- 50 Graham, R. S.; Likhtman, A. E.; McLeish, T. C. B. *J. Rheol.* **2003**, *47*, 1171–1200.
- 51 Osaki, K.; Inoue, T.; Uematsu, T. *J. Polym. Sci. Part B: Polym. Phys.* **2000**, *38*, 3271–3276.
- 52 Chow, A.; Keller, A.; Muller, A. J.; Odell, J. A. *Macromolecules* **1988**, *21*, 250–256.
- 53 Doi, M.; Edwards, S. F. *The Theory of Polymer Dynamic*; Oxford University Press: Oxford, **1986**.
- 54 Dror, Y.; Salalha, W.; Avrahami, R.; Zussman, E.; Yarin, A. L.; Dersch, R.; Greiner, A.; Wendorff, J. H. *Small* **2007**, *3*, 1064–1073.
- 55 Zussman, E.; Chen, X.; Ding, W.; Calabri, L.; Dikin, D. A.; Quintana, J. P.; Ruoff, R. S. *Carbon* **2005**, *43*, 2175–2185.
- 56 Sun, Z. C.; Zussman, E.; Yarin, A. L.; Wendorff, J. H.; Greiner, A. *Adv. Mater.* **2003**, *15*, 1929–1936.
- 57 Arinstein, A.; Zussman, E. *Phys. Rev. E* **2007**, *76*, 056303 1–7.
- 58 Arinstein, A.; Avrahami, R.; Zussman, E. *J. Phys. D Appl. Phys.* **2009**, *42*, 015507, 1–7.
- 59 Peng, Y.; Wu, P. Y.; Yang, Y. L. *J. Chem. Phys.* **2003**, *119*, 8075–8079.
- 60 Miller, R. E.; Shenoy, V. B. *Nanotechnology* **2000**, *11*, 139–147.
- 61 Sharma, P.; Ganti, S.; Bhate, N. *Appl. Phys. Lett.* **2003**, *82*, 535–537.
- 62 Cammarata, R. C. *Prog. Surf. Sci.* **1994**, *46*, 1–38.
- 63 Buell, S.; Van Vliet, K. J.; Rutledge, G. C. *Macromolecules* **2009**, *42*, 4887–4895.
- 64 Tan, E. P. S.; Lim, C. T. *Compos. Sci. Technol.* **2006**, *66*, 1102–1111.
- 65 McKenna, G. B. Confit III. *Eur. Phys. J. Spec. Top.* **2007**, *141*, 291–301.
- 66 Keddie, J. L.; Jones, R. A. L.; Cory, R. A. *Europhys. Lett.* **1994**, *27*, 59–64.
- 67 Dalnoki-Veress, K.; Forrest, J. A.; Murray, C.; Gigault, C.; Dutcher, J. R. *Phys. Rev. E* **2001**, *63*.
- 68 vanZanten, J. H.; Wallace, W. E.; Wu, W. L. *Phys. Rev. E* **1996**, *53*, R2053–R2056.
- 69 Reiter, G. *Macromolecules* **1994**, *27*, 3046–3052.
- 70 Brown, H. R.; Russell, T. P. *Macromolecules* **1996**, *29*, 798–800.
- 71 Kajiyama, T.; Tanaka, K.; Takahara, A. *Macromolecules* **1997**, *30*, 280–285.
- 72 Tanaka, K.; Taura, A.; Ge, S. R.; Takahara, A.; Kajiyama, T. *Macromolecules* **1996**, *29*, 3040–3042.
- 73 Fujii, Y.; Akabori, K. I.; Tanaka, K.; Nagamura, T. *Polym. J.* **2007**, *39*, 928–934.
- 74 Cuenot, S.; Fretigny, C.; Demoustier-Champagne, S.; Nysten, B. *Phys. Rev. B* **2004**, *69*, 165410, 1–5.
- 75 Dingreville, R.; Qu, J. M.; Cherkaoui, M. J. *Mech. Phys. Solids* **2005**, *53*, 1827–1854.
- 76 Zussman, E.; Burman, M.; Yarin, A. L.; Khalfin, R.; Cohen, Y. *J. Polym. Sci. Part B: Polym. Phys.* **2006**, *44*, 1482–1489.
- 77 Xu, S. H.; O’Connell, P. A.; McKenna, G. B. *J. Chem. Phys.* **2010**, *132*, 184902, 1–9.
- 78 Arinstein, A. *Soviet Phys. JETP* **2000**, *91*, 206–225.
- 79 Arinstein, A. E. In *Models of Directed Self-Avoiding Walks and Statistics of Rigid Polymer Molecules*; Uvarova, L., Ed.; Kulwer Academic/Plenum Publisher: Moscow, **2001**.
- 80 Mezikovskii, S. M.; Arinstein, A. E.; Deberdeev, R. J.; Zaikov, G. E. *The Oligomeric State of Substances*; Nova Publishers: Moscow, **2009**.
- 81 Onsager, L. *Ann. N.Y. Acad. Sci.* **1949**, *51*, 627–659.
- 82 Neway, B.; Westberg, A.; Mattozzi, A.; Hedenqvist, M. S.; Baschetti, M. G.; Mathot, V. B. F.; Gedde, U. W. *Polymer* **2004**, *45*, 3913–3922.